Accepted Manuscript

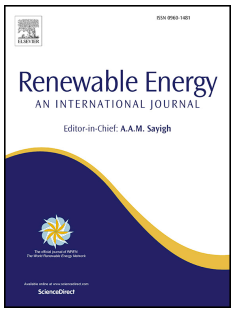

A fundamental coupling methodology for modeling near-field and far-field wave effects of floating structures and wave energy devices

Vasiliki Stratigaki, Peter Troch, David Forehand

PII: S0960-1481(19)30708-6

DOI: https://doi.org/10.1016/j.renene.2019.05.046

Reference: RENE 11638

To appear in: *Renewable Energy*

Received Date: 26 November 2018

Revised Date: 17 April 2019

Accepted Date: 12 May 2019

Please cite this article as: Stratigaki V, Troch P, Forehand D, A fundamental coupling methodology for modeling near-field and far-field wave effects of floating structures and wave energy devices, *Renewable Energy* (2019), doi: https://doi.org/10.1016/j.renene.2019.05.046.

A FUNDAMENTAL COUPLING METHODOLOGY FOR MODELING NEAR-FIELD AND FAR-FIELD WAVE EFFECTS OF FLOATING STRUCTURES AND WAVE ENERGY DEVICES

Vasiliki Stratigaki*[1], Peter Troch[1], David Forehand[2]

ABSTRACT

This research focuses on the numerical modeling of wave fields around (oscillating) structures such as wave energy converters (WECs), to study both near and far field WEC effects. As a result of the interaction between oscillating WECs and the incident wave field, additional wave fields are generated: the radiated and the diffracted wave field around each WEC. These additional wave fields, together with the incident wave field, make up the perturbed wave field. Several numerical methods are employed to analyse these wave fields around WECs. For example, for investigating wave-structure (wave-WEC) interactions, wave energy absorption and near field effects, the commonly used and most suitable models are based on Boundary Element Methods for solving the potential flow formulation, or models based on the Navier-Stokes equations. These models are here referred to as 'wave-structure interaction solvers'. On the other hand, for investigating far field effects of WEC farms in large areas, wave propagation models are most suitable and commonly employed. However, all these models suffer from a common problem; they cannot be used to model simultaneously both near and far field effects due to limitations.

In this paper, a generic coupling methodology is presented, developed to combine the advantages of the above two approaches; (a) the approach of wave-structure interaction solvers, which are used to investigate near field effects because they can more correctly model wave energy absorption and the resulting wave fields induced by oscillating WECs or WEC farms. These solvers suffer from high computational cost and thus are mainly used for limited: (i) areas around WECs; (ii) number of WECs, and (b) the approach of wave propagation models, which are used for predicting far field effects and which can model the effect of WEC farms on the wave field and the shoreline in a cost-effective manner, but usually cannot deliver high-fidelity results on wave energy absorption by the WECs.

[1]Department of Civil Engineering, Ghent University, Technologiepark 60, Ghent, B-9052, Belgium
*Corresponding author. Tel. +32(0)9/264.54.89; fax: +32(0)9/264.58.37
E-mail addresses: Vasiliki.Stratigaki@UGent.be (V. Stratigaki); Peter.Troch@UGent.be (P. Troch)
Address Department of Civil Engineering, Ghent University, Technologiepark 60, Ghent, B-9052, Belgium.
[2]Institute for Energy Systems, Institute for Energy Systems, The University of Edinburgh, The King's Buildings, Edinburgh, EH9 3JL, United Kingdom; E-mail address: D.Forehand@ed.ac.uk (D.Forehand);

In addition, a novel wave generation technique is presented, for generating the perturbed wave field induced by an oscillating WEC, in a wave propagation model. The results obtained from the proposed coupling methodology and wave generation technique along a circle are validated and show very good agreement. Finally, the benefits of the proposed coupling methodology to model floating bodies in a phase resolving wave propagation model are discussed.

Keywords: numerical coupling methodology; wave generation on a circle; wave-structure interactions; Wave Energy Converters; floating structures; WEC arrays;

Index of Abbreviations and Acronyms:

AEP: Annual Energy Production

BEM: Boundary Element Methods

CFD: Computational Fluid Dynamics

DOF: Degrees Of Freedom

NS: Navier-Stokes

PTO: Power-Take-Off

SWAN: Simulating WAves Nearshore (acronym)

WAMIT: WaveAnalysisMIT (acronym). WAMIT was developed by researchers at Massachusetts Institute of Technology.

WEC: Wave Energy Converter

1 INTRODUCTION

1.1 WAVE FIELDS AROUND OSCILLATING STRUCTURES

The operation of a wave energy converter (abbreviated as WEC) is based on the principle that a WEC interacts with the incident waves and absorbs a certain amount of energy from them.

In the case of a stationary WEC (the WEC does not move under wave action), the incident waves are partly reflected from, diffracted around and transmitted under the WEC, and no wave power is absorbed. When the WEC oscillates, an additional radiated wave field is generated. In that case, the WEC absorbs wave power (through the so-called ‘power-take-off-system” abbreviated as “PTO-system”) by generating a wave.

Linear theory is often used to model wave-structure interaction and therefore the generated wave fields can be separated by applying the superposition principle. The superposition of the (i) incident,

the (ii) diffracted and the (iii) radiated wave fields results in the 'perturbed wave field' around the WEC (Falnes, 1997). For an incident plane wave propagating in one direction, the shape of the diffracted and radiated waves is altered and the resulting perturbed waves propagate in every direction from the oscillating WEC.

In order to extract a considerable quantity of wave power from the incident waves, large numbers of WECs will have to be arranged in "arrays" or "farms" using a particular geometrical configuration. In a WEC farm, additional hydrodynamic interactions take place between neighbouring WECs (so-called "near field effects"), and therefore the wave fields around these WECs interfere with each other. As a result, the overall power output of the WEC farm is affected and is therefore not equal to the sum of the power output from the individual WECs.

In addition, the wave field at large distances behind WEC farms is typically a region of reduced wave energy density and wave heights. These are the so-called "far field effects" which may influence coastal processes, neighbouring activities and other users in the sea, other marine energy projects, coastal eco-systems and even the coastline and the coastal defence conditions and parameters.

1.2 NUMERICAL MODELLING OF WEC (FARM) EFFECTS

A numerical methodology for the combined accurate prediction of both near and far field effects (herein referred to as "WEC effects", or "WEC farm effects" when multiple WECs are considered) is the main focus of the present research. A generic coupling methodology is here presented for combining the approaches used for investigating near and far field WEC (farm) effects.

For simulating near field effects and wave energy absorption by WECs, the most commonly used models are based on the Boundary Element Methods (abbreviated as BEM) approach of potential flow theory. These models (e.g. Aquaplus (Delhommeau, 1987), ANSYS Aqwa (www.ansys.com), WAMIT (www.wamit.com)) have been used for small computational domains and small WEC arrays of up to 10 WECs (Mavrakos and McIver, 1997; De Backer et al., 2010; Vicente et al., 2009) and only for constant water depths (e.g. WAMIT, NEMOH (Babarit & Delhommeau, 2015). However, due to a better description of the related physics as presented by Yu and Li (2013), the use of codes resolving the Navier-Stokes (abbreviated as "NS") equations (e.g. Computational Fluid Dynamics (CFD) models, or Smoothed Particle Hydrodynamics (SPH) methods) for modeling WECs, is growing (Westphalen et al., 2009, Agamloh et al., 2008; Finnegan and Goggins, 2012;

Crespo et al., 2018; Devolder et al., 2018). Such BEM- and NS-based solvers will be herein referred to as "wave-structure interaction solvers".

For simulating far field effects, the approach of wave propagation models is employed. Within these, a WEC is represented in a simplified way, by a porous structure that extracts a specific quantity of wave power. The simulated WEC exhibits a specific amount of reflection, transmission and absorption of the incident waves. Spectral wave propagation models, e.g. SWAN (Booij et al., 2007) and Boussinesq models, e.g. MIKE21 BW (Madsen and Sørensen, 1992) have both been employed to study the change of shoreline waves due to the installation of a WEC farm near a shoreline (e.g. Millar et al., 2006, Venugopal and Smith, 2007; Alexandre et al., 2009; González-Santamaría et al., 2012; O'Dea et al., 2014; Chang et al., 2016). Far field effects in the lee of a WEC farm have been studied by Beels et al. (2010a; 2010b) by using the mild-slope wave propagation model MILDwave (Troch, 1998), resulting in guidelines for optimal WEC farm geometric lay-outs. Later studies provided modified formulations for wave propagation models, such as for MILDwave (Beels, 2010c, Troch et al., 2010) and SWAN (Smith et al. 2012; Ruehl, et al., 2013) to enable frequency-dependent wave energy transmission through an 'obstacle' or a 'barrier' as often WECs are referred to (and thus modelled) in wave propagation models. Recently Luczko et al. (2018) developed SWAN modelling and accounted for the WEC output power and energy dissipated through hydrodynamic drag and moorings.

All of the above mentioned models suffer, though, from a common problem; these cannot be used to model both near and far field effects, as reviewed by Folley et al. (2012) and Li and Yu (2012).

The limitations of the simultaneous modelling of WEC (farm) effects are here summarized.

Wave-structure interaction solvers suffer from a high computational cost, when simulating power absorption and the wave field alteration due to large WEC farms. Large simulation domains of non-constant water depth are prohibitive, which results also in restrictions on the number of the simulated WECs. However, in order to investigate far field effects in real WEC farm installation sites, for example to study coastal impact, much larger computational domains are required where the local bathymetries can be represented.

On the other hand, the approach of wave propagation models does enable simulation of far field effects. Large WEC farms installed in large domains (several tens of kilometers) are modelled at a reasonable computational cost. As a result, the changes in wave field and the associated environmental impacts can be studied at regional scale. However, the WECs are often approximated

by using parameterized energy sinks and empirically tuned energy absorption coefficients. This method only partially addresses the underlying physics, which may lead to erroneous model conclusions. Moreover, when it comes to the modeling of oscillating WECs, the radiated wave field induced by the WECs' motion is not considered in wave propagation models such as in the studies by Vidal et al., 2007; Mendes et al., 2008; and Le Crom et al., 2008, as well as in the review study by Tuba Özkan-Haller et al. (2017) who compared the performance of WAMIT and SWAN in WEC array modeling.

In Folley et al. (2012), the metrics of characteristics for fundamental modelling, computational processing and model usability are used for a comparative analysis of the numerical techniques that are most commonly employed to model WEC farms. Based on these metrics, the suitability of each numerical technique is evaluated for a range of different modelling tasks. These include investigation of near field effects, estimation of annual energy production (AEP) and assessment of distal environmental impacts (far field effects).

As a result of the analysis presented in Folley et al. (2012), models based on the BEM approach of linearized potential flow theory are suitable for modeling near field hydrodynamic interactions in the vicinity of large WECs in deep water, that shed minimal vortices. When localized effects such as vortex shedding (viscous effects) behind an oscillating WEC, wave overtopping and the re-entering impact of an-out-of-water body are important, the approach of NS solvers is the most suitable. Whilst Boussinesq/mild-slope models resolve phase, they are unlikely to accurately model the near field and the wave-WEC interaction, and so are poorly suited.

Regarding AEP, linear BEM-based models, rapidly become unsuitable for that purpose as the number of WECs increases, due to the quadratic relationship between the computational effort and the number of WECs. Similarly, the approach of CFD models resolving the NS equations is not suitable due to high computational requirements. The Boussinesq/mild-slope and spectral models are highly efficient in calculating the AEP.

Concerning suitability for determining far field effects: none of the BEM models are suitable because of the assumption of constant water depth. This assumption does not allow wave propagation to the shoreline, where the environmental impact is typically most significant. Furthermore, the large wave propagation distances make CFD models poorly suited due to their high computational requirements. Boussinesq/mild-slope and spectral models are highly suitable for

determining environmental impact and have been used extensively for this task in many applications besides in the wave energy field.

In the present paper, an innovative numerical coupling methodology for predicting WEC farm effects is presented. This coupling methodology has been developed to combine:

(i) the advantages of the approach of wave-structure interaction solvers, which accurately formulate and efficiently resolve the physical processes in wave energy absorption; and,

(ii) the benefits of the approach of wave propagation models, which efficiently resolve the propagation and transformation of waves over large distances, including bathymetric variability over the WEC farm area and wave transformation processes when approaching the coastline.

Moreover, a novel wave generation technique is presented used for generating the perturbed or radiated wave field induced by an oscillating WEC or other floating structures in a wave propagation model. The WEC is implemented using prescribed internal boundary wave conditions, imposed on a wave generation circle which surrounds the WEC.

Up to now, the coupling methodology using the technique presented in this paper, is the first coupling of this kind found in literature.

1.3 PAPER OVERVIEW

The proposed coupling methodology is illustrated here by its implementation in the wave propagation model, MILDwave (Troch, 1998), and verified against wave field results obtained by the wave-structure interaction solver and frequency domain code, WAMIT (www.wamit.com). Therefore, the test case used to verify the proposed coupling methodology, illustrates the coupling between the BEM approach of linearized flow theory and the approach of a time domain wave propagation model.

The details of the proposed coupling methodology are presented in Sections 2 and 3 with clear illustrations of the step-by-step procedure. Two schemes are presented for modeling the resulting wave field due to interaction between a WEC and waves: (i) that of a generic coupling between any wave-structure interaction solver and any wave propagation model, and, (ii) a scheme for coupling between the two selected models, for the case of an individual heaving WEC. At the end of Section 3, the step-by-step technique is presented, developed to model multiple WECs (or WEC farms) by using the proposed coupling methodology. Section 3, provides information on MILDwave and WAMIT which are here used to demonstrate the coupling, as well as the details of the developed

wave generation technique on a wave generation circle. In Section 4, the implementation of the proposed coupling methodology is reported, for a benchmarking test case. First the characteristics are briefly mentioned of the modeled test case (an individual heaving WEC). Then the diffracted, radiated and perturbed wave fields around the WEC are modeled, using WAMIT. This simulations provide also the prescribed internal boundary wave conditions on the wave generation circle, which is used in the proposed coupling methodology to generate the radiated wave field around the WEC. Furthermore, the diffracted, radiated and perturbed wave field around the WEC are also modeled in the wave propagation model MILDwave in which the proposed coupling methodology is used. Section 5, provides the verification results of the proposed coupling methodology against wave field results from WAMIT. The agreement between the results from the proposed coupling methodology and those obtained by the wave-structure solver is evaluated and discussed. This discussion is carried out first for the diffracted and radiated wave fields around the WEC separately, and then for the perturbed wave field.

Finally, a summary of the presented study, the verification results and the obtained conclusions, is presented in Section 6. Also the potential of the proposed coupling methodology and its benefits is addressed.

2 STEP-BY-STEP PROCEDURE OF IMPLEMENTING THE PROPOSED COUPLING METHODOLOGY: THE GENERIC CASE

The proposed coupling methodology is generic, as:

(i) any wave-structure solver or analytical expression describing the perturbed wave field (e.g. the so called Kochin function (Wang, 1986; Mei et al., 2005; Babarit et al., 2013)) can be used to provide the perturbed wave field used as prescribed internal boundary wave conditions. This perturbed wave field is imposed on the wave generation circle around the WEC.

(ii) any wave propagation model can be used; the wave generation circle (internal wave generation boundary) can be implemented in the numerical domain of any wave model, in both phase resolving and phase averaging models.

(iii) it applies to any fixed or oscillating/floating structure; in this paper, a heaving WEC has been selected for the verification test case, but the same methodology is applied to e.g. offshore structures, WECs, oscillating water columns, floating breakwaters, platforms, etc.

(iv) by using this coupling methodology, it is possible to model the resulting wave fields around structures which have from 0 (fixed) to all 6 Degrees of Freedom (abbreviated as “DOF”).

The proposed generic coupling methodology, as illustrated in Fig. 1a, consists of three steps:

1. Step 1: Firstly, the wave propagation model is used to obtain the incident wave field at the location of the structure(s) of interest.
2. Step 2: Secondly, the obtained incident wave field from 'Step 1' is used as input in the wave-structure interaction solver to receive an accurate solution of the perturbed wave field around the structure. The resulting perturbed wave field information along a circle that surrounds the structure, is used then in the next step.
3. Step 3: Thirdly, the perturbed wave field information from 'Step 2' is used as input in the wave propagation model. The perturbed wave field is imposed as prescribed internal boundary wave conditions on a wave generation circle which surrounds the structure, as shown in Fig.2a.
4. Step 4: Using the wave propagation model, the far field perturbed waves (including the diffracted, and if applicable, the radiated wave fields) are calculated. This is the last step of the procedure described in Fig. 1a.

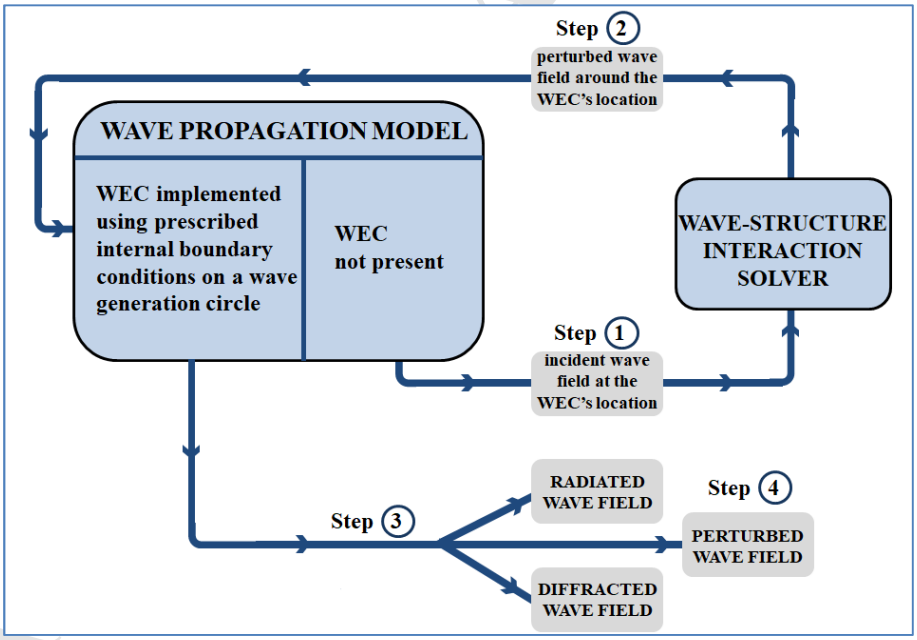

a)

b)

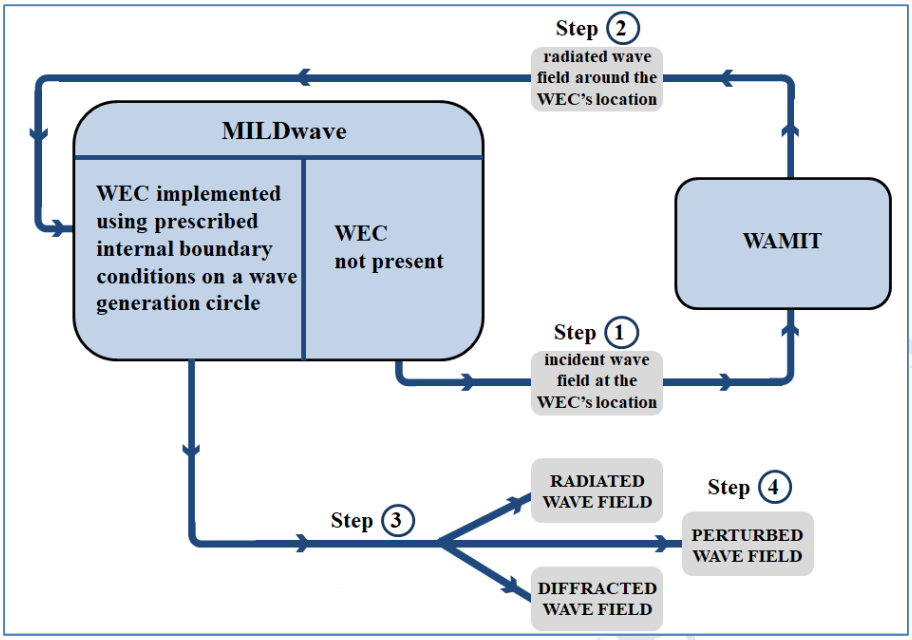

Figure 1. Flow chart illustrating the step-by-step procedure for realizing the proposed coupling methodology used for predicting near and far field WEC (farm) effects: a) generic case for coupling between the approaches of a wave–structure interaction solver and a wave propagation model; b) demonstration for coupling between the models WAMIT and MILDwave..

In this way, the resulting far field effects of a WEC or a floating structure can be further modeled using the wave propagation model. This allows for time-efficient and accurate modelling, taking into account both the geometric/bathymetric characteristics and wave transformation at the installation site, as well as the detailed perturbed wave field around the structure.

Figure 2a represents the numerical domain in the wave propagation model when the proposed coupling methodology is used. Incident waves are generated along the offshore wave generation boundary at the edge of the domain. The structure is implemented using the wave generation circle upon which prescribed internal boundary wave conditions are imposed, for the perturbed wave field. In the area within the wave generation circle, a wave absorbing sponge layer is used to avoid undesirable interferences for the generated wave field. The numerical details of the proposed wave generation technique on a circle are presented in Section 3.1.2.2.

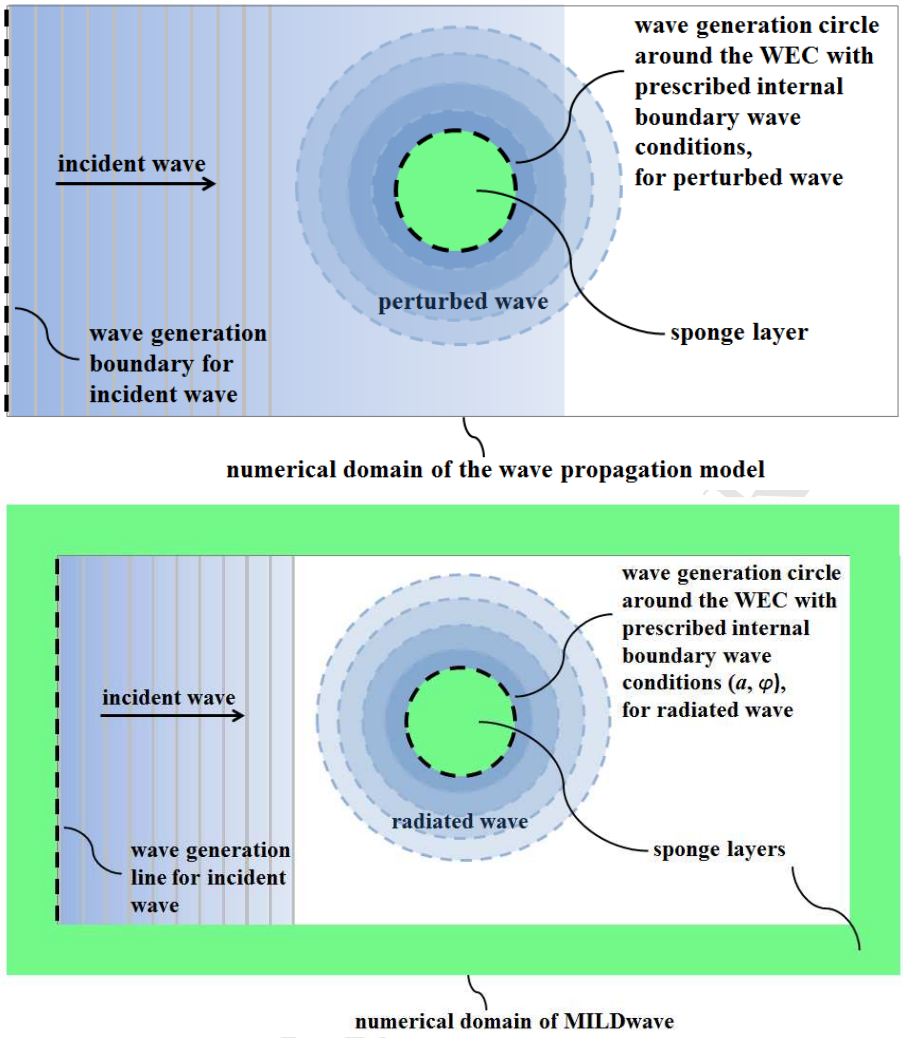

Figure 2. Definition sketch of the technique of the wave generation on a circle around the WEC. The wave generation boundary for the incident wave field is also presented. a) Generic case: prescribed internal boundary wave conditions are used for the perturbed wave field around the WEC. The perturbed wave field around the WEC is derived from a wave-structure interaction solver; b) demonstration for the model, MILDwave: the radiated wave field around the heaving WEC is used as prescribed internal boundary wave conditions, which is derived from WAMIT.

3 STEP-BY-STEP PROCEDURE OF THE PROPOSED COUPLING METHODOLOGY: DEMONSTRATION BASED ON A TEST CASE

3.1 INTRODUCTION IN NUMERICAL MODELS AND TEST CASE EMPLOYED

As an example of the implementation and validation of the proposed generic coupling methodology described in Section 2, a validation test case has been set-up:

- the ‘structure’ causing the perturbed wave field is represented by an axi-symmetric cylindrical heaving WEC with one DOF;

- the selected wave-structure interaction solver is WAMIT (www.wamit.com);
- the selected wave propagation model is MILDwave (Troch, 1998).

In the presented test case, WAMIT output is used as input on the wave propagation circle for implementing the coupling methodology in MILDwave.

First, the hydrodynamic interaction between the heaving WEC and the incident wave field is modeled using WAMIT. No damping is applied on the WEC through the PTO-system and therefore the results presented here refer to a freely heaving WEC (undamped heave motion) in order to demonstrate the wide applicability of the coupling methodology for any floating structure.

A detailed description of the WEC geometry, response and power-take off system is provided in Stratigaki et al. (2014). In summary, the WEC consists of a buoy (Fig. 3), with hemispherical bottom and a cylindrical vertical body (total height of 60.0 cm). The buoy's draft is 31.5 cm, equal to its diameter, *D*, with a total mass, m = 20.490 kg. Note that the radius of the axi-symmetric WEC is r_b = 0.1575 m. The coordinates of the WEC centre (x_C, y_C) coincide with the centre of the internal wave generation circle, and with the centre of the used numerical domains.

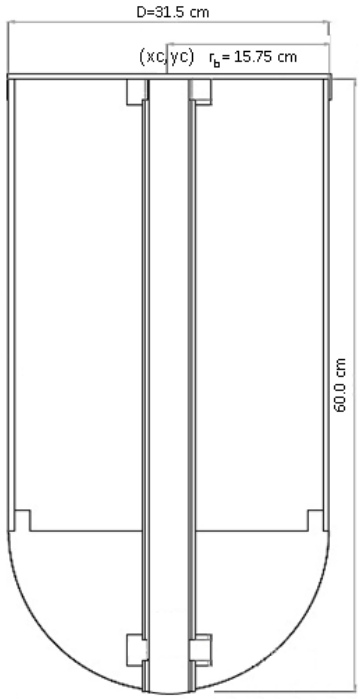

Figure 3. Dimensions of the WEC buoy.

3.1.1 SHORT DESCRIPTION OF WAMIT AND MILDWAVE

To model the interaction of an individual WEC with the incident wave field, the BEM approach of linearized potential flow is used (WAMIT). A brief description of the equations used in the potential flow methods, is given e.g. in Folley et al. (2012), as well as its limitations as linear solver. The assumptions, upon which WAMIT is based, are the small amplitude of motions and small wave steepness, as well as the assumption of uniform water depth and thus, of a constant bathymetry.

3.1.2 SHORT DESCRIPTION OF MILDwave

The phase-resolving model MILDwave (Stratigaki and Troch, 2012) is a mild-slope wave propagation model developed by Troch (1998). MILDwave is able to generate linear water waves over a mildly varying bathymetry. Bathymetries can be modelled accurately, since the model has mostly been applied for fine grid cell sizes. The model calculates instantaneous surface elevations throughout the domain, with a relatively low computational and accuracy cost and with a high stability performance.

Wave transformation processes such as refraction, shoaling, reflection, transmission, diffraction are simulated intrinsically, including wave breaking and wave growth by wind (Stratigaki et al., 2011). The model can generate regular and irregular long- and short-crested waves. In MILDwave, far field effects in the lee of farms composed of WECs of the overtopping type (e.g. the Wave Dragon WEC, Beels, 2009; 2010b) and energy absorption have been extensively studied (e.g. Troch et al., 2010; Beels et al. 2010a; 2010b; 2010c; Stratigaki et al., 2011, Folley et al., 2012).

MILDwave makes use of the hyperbolic mild-slope equations of Radder and Dingemans (1985). For regular waves, these equations are expressed by Eq. (1):

$$\frac{\partial \eta}{\partial t} = \frac{\omega^2 - k^2 C C_g}{g}\phi - \nabla \cdot \left(\frac{C C_g}{g}\nabla\phi\right)$$

$$\frac{\partial \phi}{\partial t} = -g\eta \qquad (1)$$

where η *and* ϕ are respectively the surface elevation and the velocity potential at the free water surface, ∇ is the horizontal gradient operator, t is the time, g is the gravitational acceleration, C is the phase velocity and C_g the group velocity for a wave with wave number, k_w, angular frequency, ω, wavelength, L and frequency, f. A derivation of these equations can be found in Radder and

Dingemans (1985). For irregular waves, C, C_g, k_w and ω are replaced in Eq. (1) by the wave characteristics for the carrier frequency $\bar{f}$, i.e. $\bar{C}$, $\overline{C_g}$, $\overline{k_w}$and $\bar{\omega}$.

3.1.2.1 Wave generation on a line and on an arc

In MILDwave, waves are typically generated at the offshore boundary by using the source term method, i.e. by adding an additional surface elevation, η^*, to the calculated value on a wave generation line (Lee and Suh, 1998) or wave generation arc (Lee and Yoon, 2007) for each time step.

The additional surface elevation, η^*, on a wave generation line for generating waves with wave direction, θ, in deep and shallow water, is given by Eq. (2) for a wave generation line parallel to the y-direction, and by Eq. (3) for a wave generation line parallel to the x-direction:

$$\eta^* = 2\eta_i \frac{C_e \Delta t}{\Delta x} \cos\theta \qquad (2)$$

$$\eta^* = 2\eta_i \frac{C_e \Delta t}{\Delta y} \cos\theta \qquad (3)$$

with $\eta_i = a\sin(\omega t)$ being the surface elevation of the incident waves (where the subscript "i" refers to incident waves, a, is the wave amplitude, ω, is the angular wave frequency and, t, is the time), C_e the energy velocity, Δt the time step, Δx and Δy the grid cell size in x- and y-direction, respectively, and θ the angle of wave propagation.

3.1.2.2 Implementation of wave generation on a circle in MILDwave

Due to the motion of floating structures/breakwaters/platforms or oscillating WECs / water columns, a radiated wave field is generated. In MILDwave, the generation of the radiated wave field is implemented by introducing wave generation on a circle, based on the study by Lee and Suh (1998). This technique which has been first introduced by Beels et al. (2010a; 2010c) and implemented and optimized by Stratigaki (2014), has been afterwards adopted by Babarit et al. (2013) for modelling WECs in wave models. To generate waves on a circle with centre (x_C, y_C) and radius r_C in a rectangular grid, the circle is approximated by a discrete number of grid cells (Fig. 4). The x- and y-co-ordinates of these grid cells, in the x- and y-direction, respectively, are given by Eqs. (4) and (5) for $i \in [1, 360°/\Delta b]$. Note that iΔb = 90° represents a location behind the WEC, which is important for the diffraction problem when the WEC is also under incident waves (e.g. as shown in Figures 2a and 2b):

$$x = \left\{ floor\left[\frac{x_C + r_C \cos(i\Delta b)}{\Delta x} \right] \right\} \times \Delta x \qquad (4)$$

$$y = \left\{ floor\left[\frac{y_C + r_C \sin(i\Delta b)}{\Delta y} \right] \right\} \times \Delta y \qquad (5)$$

where the 'floor' function rounds to the largest previous integer. More precisely, $floor(x) = \lfloor x \rfloor$, is the largest integer not greater than *x*.

At first instance, the angle interval Δb is approximated by *arctan* (Δy / r_c). The additional surface elevation η^* is given by Eq. (6).

$$\eta^* = 2\eta_i \frac{C_e \Delta t}{\Delta x} \qquad (6)$$

with $\eta_i = a \sin(-\omega t)$, and here $\Delta x = \Delta y$.

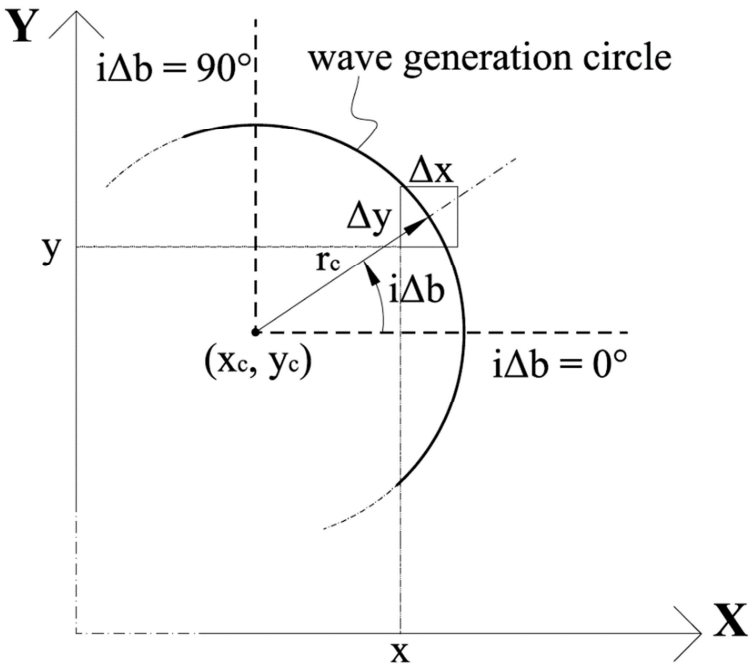

Figure 4. Definition sketch of wave generation on a circle.

Each grid cell on the wave generation circle is an individual wave generation source, which is affected by its neighbouring wave generation sources. To minimize undesirable interferences and even possibly 'double-counting' of radiated waves in the wave generation, a wave absorbing sponge layer is implemented in the inner part of the wave generation circle.

The wave generation on a circle is verified with the principle of conservation of energy for regular waves with H_{rc} and T, which are the wave height generated on a wave generation circle with radius r_C in the centre of the simulation domain (deep water conditions), and the regular wave period, respectively. The wave power on a circle with radius $r > r_C$ (where the wave height is H_r) is equal to the wave power on the wave generation circle according to the conservation of energy, as no energy sources or energy sinks are present between the two circles. The conservation of energy in deep water is expressed in Eq. (7).

$$\frac{1}{8}\rho_w g {H_{rc}}^2 C_g 2\pi r_c = \frac{1}{8}\rho_w g {H_r}^2 C_g 2\pi r \tag{7}$$

with H_r the wave height on a circle with radius $r \geq r_c$, as illustrated in the definition sketch of Figure 5. Equation (7) yields the ratio H_r / H_{rc}:

$$\frac{H_r}{H_{rc}} = \frac{\sqrt{r_c}}{\sqrt{r}} \tag{8}$$

The ratio H_r / H_{rc} has a starting value of 1.0 for $r = r_c$, and decreases when r increases, as given by the analytical solution of Eq. (8). However in MILDwave, it was observed that the obtained ratio receives too high values (with e.g. a starting value for H_r / $H_{rc} \neq 1.0$). This may occur due to the grid cell discretization along the wave generation circle: MILDwave is based on rectangular grid discretization, and thus the circle is approximated. Moreover, too much destructive interference occur on the wave generation circle by using the approximated value of the angle interval Δb ($arctan\ (\Delta y / r_c)$), due to mutual influences of the wave generation sources on the wave generation circle and due to the used sponge layer characteristics inside the wave generation circle. On the other hand, as shown later in Figure 9, the selection of a too fine Δb results in generation of too much energy by the individual wave generation sources on the wave generation circle. Therefore an iterative approach is used to define the value of the angle interval Δb, for achieving good agreement between the analytical solution of Eq. (8) and the obtained numerical results.

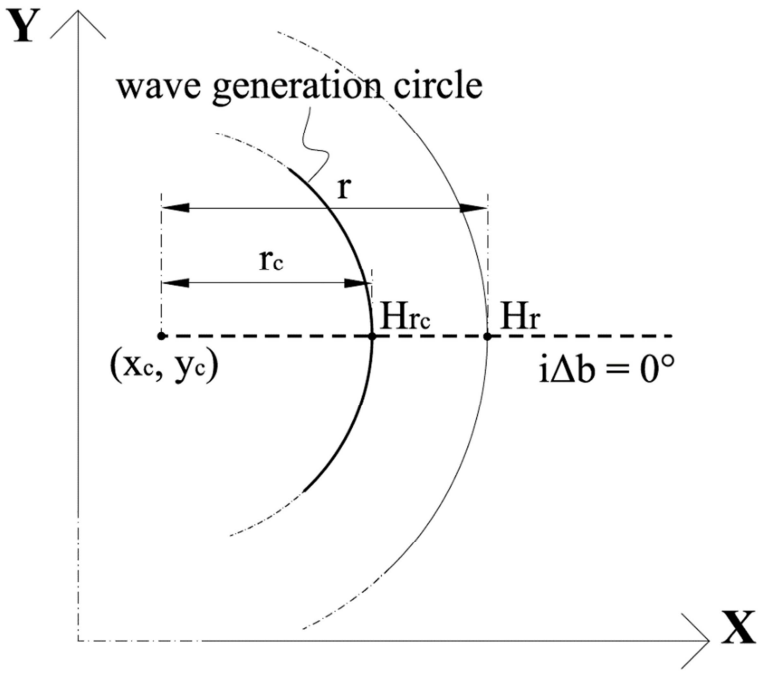

Figure 5. Definition sketch of the wave heights at radii r and r_C from the centre of the wave generation circle with coordinates (x_C, y_C).

3.2 MODELLING OF AN INDIVIDUAL HEAVING WEC

The step-by-step procedure for the proposed generic coupling methodology presented in Fig. 1a, is now adjusted in Fig. 1b by replacing in the flow chart the term “Wave propagation model” by ‘MILDwave’ and “wave-structure interaction solver” by ‘WAMIT’. Note that the only difference between the procedures of Fig. 1a and 1b is that now in MILDwave, only the radiated wave field from WAMIT is further used as input (it is used as prescribed internal boundary wave conditions along the wave generation circle). This is because diffraction around the WEC is modeled intrinsically in MILDwave and therefore only the radiated wave field from WAMIT (wave amplitude, a, and phase shift, φ, as indicated in Fig. 2b) is necessary for the implementation of the proposed coupling methodology.

In Fig. 2b, incident waves are generated along the offshore wave generation line, and then propagate from the left to the right. Simultaneously, waves are generated along the wave generation circle in the centre of the domain, simulating the radiated wave field induced by the heave motion of the WEC. The radiated waves propagate in all directions. In MILDwave, the diffracted wave field (the WEC is considered to be fixed) and the radiated wave field (the WEC is considered to heave) are calculated separately at each time step, and afterwards the wave elevations and velocity potentials are summed up. Wave absorbing sponge layers are placed along all sides of the

computational grid in MILDwave, as well as in the inner part of the wave generation circle. This is necessary, in order to avoid undesirable disturbances in the generated wave field. By separating the calculation of both wave fields, the diffracted wave is not disturbed by the wave absorbing sponge inside the wave generation circle. Moreover, the radiated wave is not disturbed by the fully reflecting structure which is used here for the simulation of the diffracted wave field. In general, a structure can be also partly wave reflecting, and thus specific absorption coefficients are assigned to the grid cells the structure occupies according to the so-called "sponge-layer" technique implemented in MILDwave by Beels et al., 2010c.

Note that when using this coupling methodology in MILDwave for modelling wave fields around other types of offshore structures and energy devices which may have up to 6 DOFs or irregular geometries, the a and φ values for the radiated wave field then will not be constant as for the here presented heaving WEC. Instead, the a and φ values will differ at each one of the discretization points on the wave generation circle and the resulting radiated wave field may be not be axi-symmetric, as that shown in Figs. 1a-b.

3.3 MODELLING OF AN ARRAY OR FARM OF OSCILLATING WECs

After implementing an individual WEC in MILDwave (Section 3.2) by using the coupling methodology, the implementation of more than one WECs (e.g. a WEC array or farm) is introduced in this section by taking into account WEC-WEC interactions.

To study a WEC farm, the diffracted wave field (all WECs of the farm are considered to be stationary) and the radiated wave field for each WEC (in first instance, every time one WEC is oscillating and the other WEC(s) are stationary) are calculated separately during each time step. This description is to illustrate the wave field summation in MILDwave, however note that the numerical implementation of each WEC's oscillation includes already the WEC-WEC interaction, e.g. due to wave diffraction, primary and secondary radiated waves, etc. Consequently, if N is the number of the WECs of the farm, at each time step N+1 wave fields are calculated and summed up as presented in Table 1 (N radiated wave fields from each WEC which include already the above mentioned WEC-WEC interactions, and 1 diffracted wave field from the entire WEC farm).

Table 1: For the coupled MILDwave model simulations in order obtain the perturbed wave field due to the presence of WECs, in each time step N+1 wave fields are calculated and summed up. For a system of WECs, the example of Figure 6 is used.

Calculated wave fields in each time step	**WEC motion**	
	WEC1	**WEC2**
Diffracted waves for all WECs	stationary	stationary
Radiated waves for WEC1	oscillates	stationary
Radiated waves for WEC1	stationary	oscillates

The radiated wave field generated by each oscillating WEC is determined in two steps. For simplicity, the methodology is illustrated here for a 'system' (or array) of two oscillating WECs, as shown in Fig. 6.

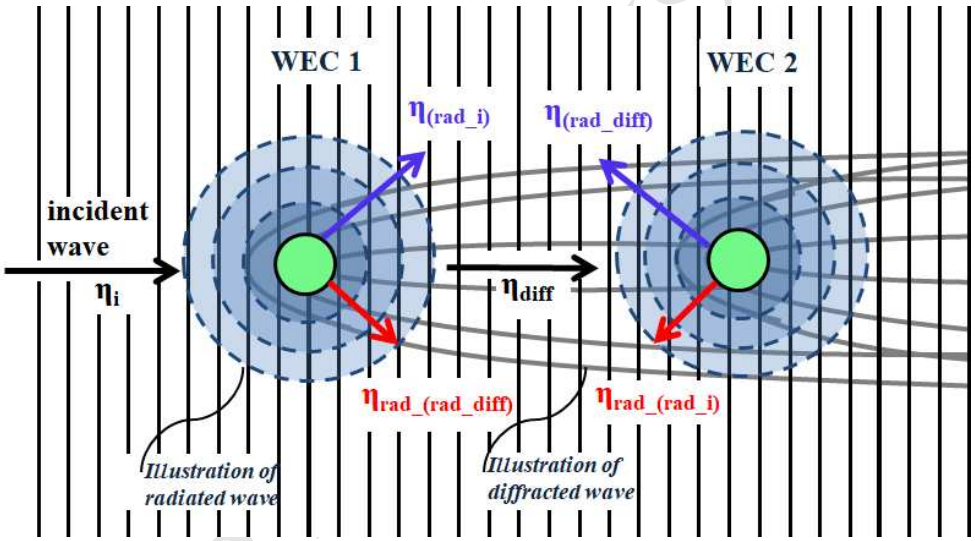

Figure 6. Definition sketch of wave field interaction for a 'system' of two oscillating WECs. The vertical black lines represent the incident waves generated along the offshore wave generation boundary at the edge (left) of the numerical domain in MILDwave. The blue circles represent the radiated waves. The curved grey lines represent the diffracted waves.

First, the wave amplitude in front of each WEC is calculated separately (i.e., for WEC1: η_i and for WEC2: η_{diff}) caused by the primary incident wave that originates from the offshore wave generation boundary in MILDwave.

Then, the amplitude of the radiated wave, a_W, as determined for an individual oscillating WEC using WAMIT, is multiplied by the wave amplitude in front of each WEC as calculated from the previous step. For WEC2, this results in the primary radiated wave, $\eta_{(rad\_diff)}$, caused by the diffracted wave. Note that in front of the first row of WECs of a farm (in Fig. 6, WEC 1), the

incident wave is not diffracted yet. Consequently, the primary radiated wave of those WECs (in Fig. 6, WEC 1), $\eta_{(rad\_i)}$, is caused by the incident wave, η_i.

As such, the secondary wave, $\eta_{rad\_(rad\_diff)}$, is generated by WEC1 due to its interaction with $\eta_{(rad\_diff)}$. Similarly, the secondary wave $\eta_{rad\_(rad\_i)}$ is generated by WEC2 due to its interaction with $\eta_{(rad\_i)}$.

The amplitude of $\eta_{rad\_(rad\_i)}$ around WEC1 is calculated by multiplying a_W by the amplitude of $\eta_{(rad\_i)}$ aroundWEC2. The amplitude of $\eta_{rad\_(rad\_diff)}$ around WEC2 is calculated by multiplying a_W with the amplitude of $\eta_{(rad\_diff)}$ around WEC1. In cases where the amplitude of these secondary radiated waves in front of the neighbouring WECs is very small compared to that of the primary incident and radiated waves, a first approach would be to neglect these secondary radiated waves. More information and details on how to apply the proposed coupling methodology in larger WEC arrays (of more than two WECs) under both regular and irregular waves is available in the study by Verao Fernandez et al. (2018) who included modelling of all WEC PTO systems and of the local bathymetry. In Figure 7, a flow chart is provided of the steps (corresponding to Steps 1-4 of Fig. 1b) followed to model WEC-WEC interactions using the example of Fig. 6 (a system of floating WECs).

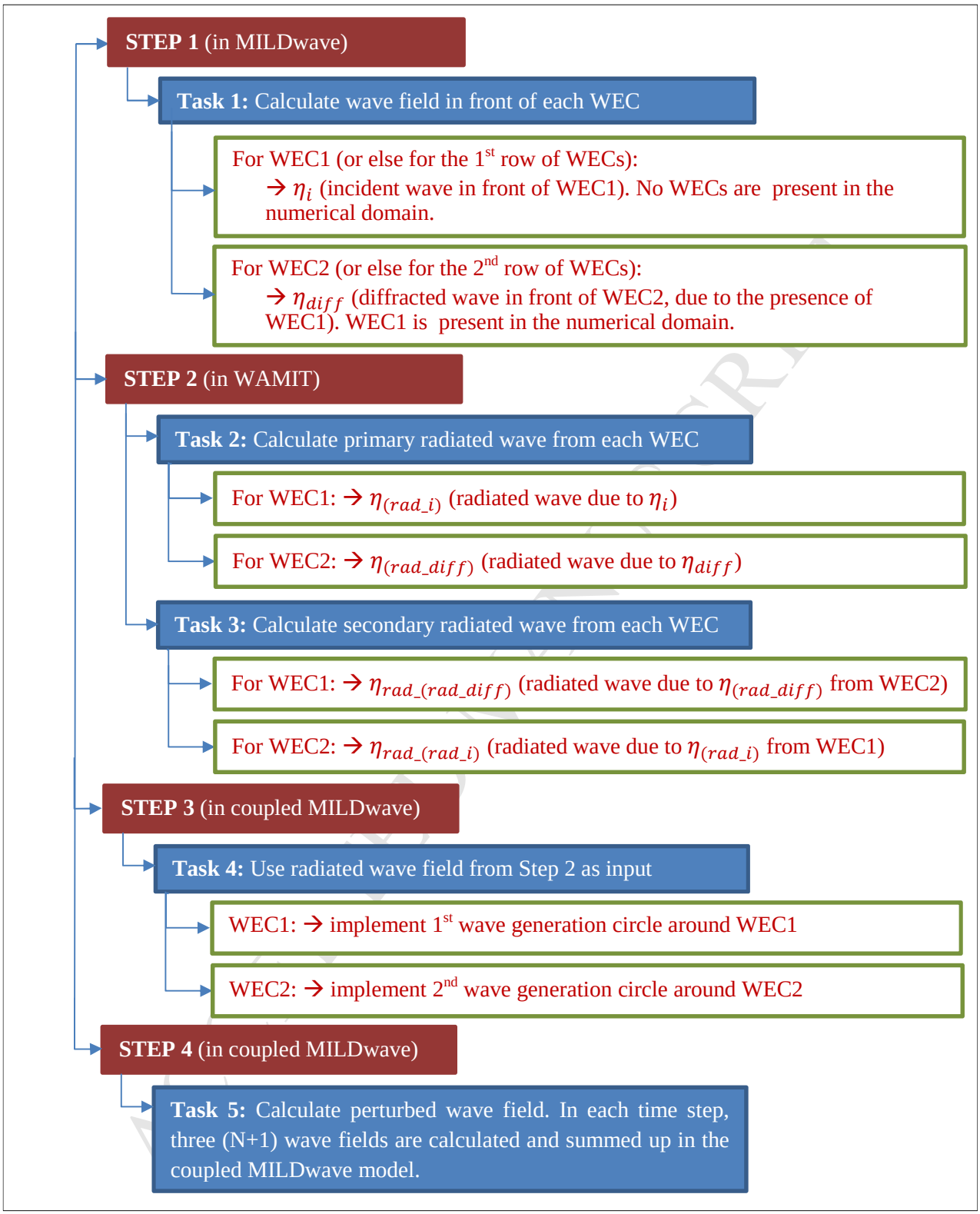

Figure 7. Flow chart of tasks for modelling the system of WECs presented in Figure 6. "STEPS 1-4" correspond to those of Figure 1b.

4 OBTAINED WAVE FIELDS AROUND A HEAVING CYLINDRICAL WEC: SOLVING THE DIFFRACTION AND RADIATION PROBLEM

4.1 BOUNDARY CONDITIONS

The wave diffraction and radiation wave fields caused by the heaving cylindrical WEC are investigated for one set of incident regular wave conditions with wave direction θ = 90°, wave amplitude a = 0.037 m, wave period T = 1.26 s, constant water depth d_w = 0.70 m and wavelength L = 2.384 m.

In MILDwave, a computational domain is defined of width 30.5L (71.9 m) in the x-direction, and of length 26L (61.4 m) in the y-direction (parallel to the incident waves of Fig. 2b with θ = 90°). An effective domain (area without the side sponge layers shown in of Fig. 2b) of 49.7 m x 39.2 m (w_d x l_d) has been modeled, using a grid cell size of Δx = Δy = 0.018 m. All MILDwave results presented here refer to steady-state.

In WAMIT, a much smaller area of 10.0 m x 10.0 m around the WEC is modeled, using a grid cell size of Δx = Δy = 0.100 m for the free-surface elevation output points. In the middle of the grid cells, the wave amplitude, a, and phase shift, φ, are calculated.

In order to make a comparison of the obtained MILDwave and WAMIT results, the same area around the WEC is considered in both models (10.0 m x 10.0 m). For the perturbed wave field (Section 4.4) a comparison is carried out for a domain with extended dimensions, 49.6 m x 39.2 m (w_d x l_d), in order to evaluate the far field effects of the WEC on the surrounding wave field.

4.2 DIFFRACTED WAVE FIELD MODELED IN WAMIT AND IN MILDWAVE

The resulting wave amplitude, a, after modelling the heaving WEC in WAMIT and in MILDwave is shown in Figs. 8a and 8b, respectively. Only diffraction is considered (both the incident and diffracted wave fields are shown). The WEC is implemented as a fully reflecting fixed structure, placed in the centre of the numerical domain (x_C, y_C).

In Fig. 8a, a ‘square’ of 3 x 3 cells is shown (thus an area of 0.3 m x 0.3 m) in the centre of the domain, where no WAMIT results are provided. Note, however, that indeed the actual WEC cylindrical geometry is used for the WAMIT calculations and therefore, the ‘missing’ cells are a result of post-processing. In this area, the values of a (and φ) are set to zero.

In MILDwave, waves are generated only along a wave generation line at the offshore boundary, which is situated along the bottom part of Fig. 8b. For the sake of simplicity, the WEC has been

modeled as a bottom based cylinder, as wave transmission is not significant in this test case. To model wave transmission in MILDwave, the so-called "sponge layer technique" developed by Beels et al. (2010a-c) is employed. In Fig. 8b, the WEC is represented by a circle with diameter, D = 0.315 m, and the values of a are zero in the grid cells occupied by the WEC.

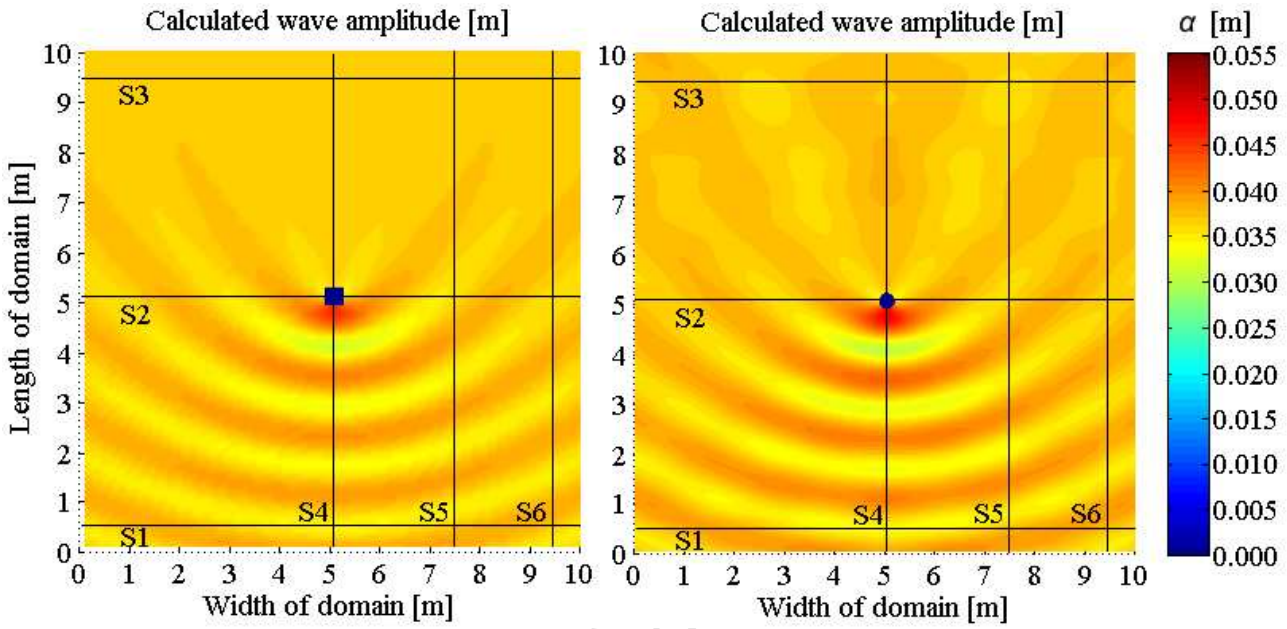

(a) WAMIT: wave amplitude, a. (b) MILDwave: wave amplitude, a.

Figure 8. Calculated wave amplitude, a, around a fixed WEC. The incident waves propagate from the bottom to the top. Both the incident and diffracted wave fields are presented. Results from: (a) WAMIT; (b) MILDwave. In MILDwave the waves are generated along a wave generation line placed far from the here presented 10.0mx10.0m part of the numerical domain.

The resulting wave field around the WEC in Figs. 8a and 8b for both numerical models shows clearly the reflected waves in front of the WEC, as well as the locally reduced wave amplitudes in the lee of the WEC. Note that the '3 x 3 cells' area of zero-values in WAMIT has slightly different dimensions and shape than the circular area occupied by the WEC in MILDwave where also a and φ are zero.

4.3 RADIATED WAVE FIELD MODELED IN WAMIT AND IN MILDWAVE

For the radiation problem, the calculated wave amplitude, a, and phase shift, φ, relative to the centre of the WEC, are shown in Figures 9(a-b) and 9(c-d), respectively,. Results are presented both from WAMIT, and from MILDwave where the internal wave generation circle has been used.

The WEC is implemented as a heaving structure, placed in the centre of the numerical domain. The propagating incident waves are not shown. In Fig. 9(a-b), the waves propagate in all directions from the source (WEC). The wave amplitude due to radiation is decreasing further away from the WEC. The contour plots of the presented results are axisymmetric, as the studied structure is an axisymmetric cylindrical heaving WEC.

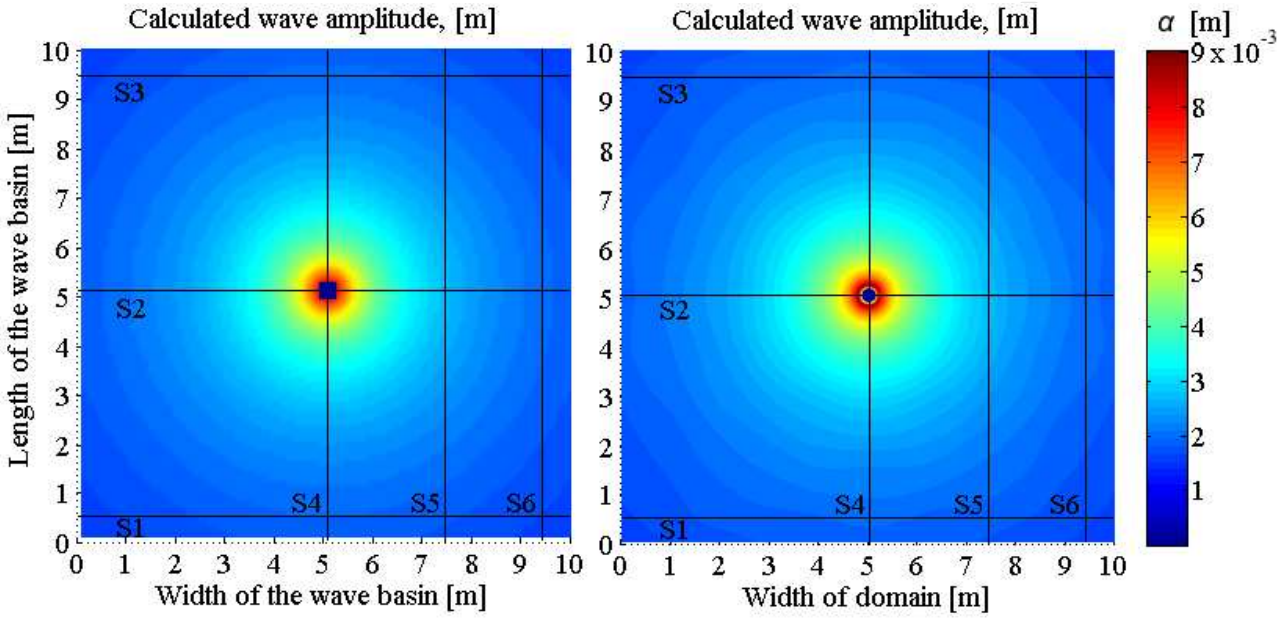

(a) WAMIT: wave amplitude, a. (b) MILDwave with wave generation circle: wave amplitude, a.

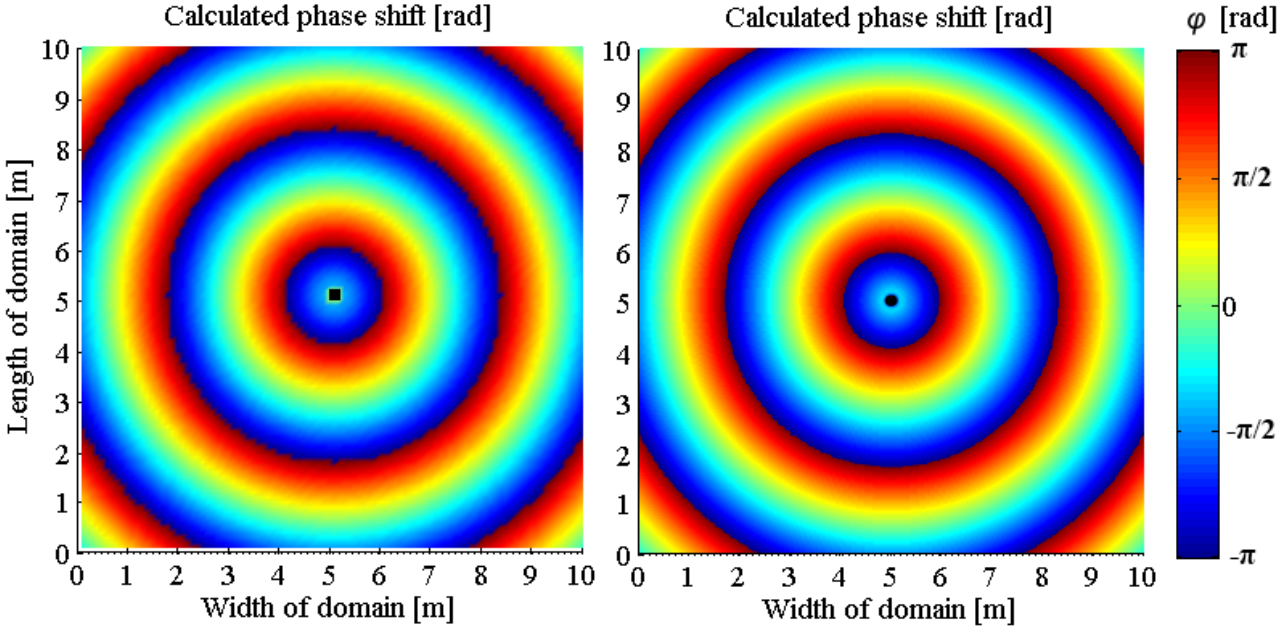

(c) WAMIT: phase shift, φ. (d) MILDwave with wave generation circle: phase shift, φ.

Figure 9. Radiated wave field around the heaving cylindrical WEC. No propagating incident waves are shown. Calculated (a-b) wave amplitude, a, and (c-d) phase shift, φ, in WAMIT, and in MILDwave where the internal wave generation circle is used, respectively. The radiated waves propagate in all directions from the source (WEC).

4.3.1 Implementation of wave generation on a circle and coupling methodology for wave radiation by the heaving WEC in MILDwave

In MILDwave, the radiated waves are generated only on a circle using the wave generation technique described in Section 3.1.2.2. For the iterative approach used to determine the angle interval, Δb, the term q is employed, defined as the ratio $a_{r,M}$ / $a_{r,W}$. $a_{r,M}$ and $a_{r,W}$ are the wave amplitudes of the radiated wave field on a radius r from the WEC centre, calculated using MILDwave and WAMIT, respectively. The $a_{r,M}$ values are obtained by using prescribed internal boundary wave conditions on a wave generation circle with centre (x_c, y_c) and radius r_c = 0.2 m (slightly larger than r_b). This circle that has been defined around the WEC within the rectangular MILDwave simulation grid. The results inside the circular area with radius $r < r_C$ are set to zero; these values have no physical meaning, as this area corresponds to the wave absorbing sponge layer illustrated in Fig. 2b.

The prescribed internal boundary wave conditions are $a_{r,W}$ and φ values which derive from the WAMIT a and φ output data of Fig. 9(a) and Fig. 9(c), respectively, taken from a radial section when $i\Delta b$ = 0° (see Fig. 5 for convention of angle interval along the wave generation circle).

In Fig. 10, the resulting q values as a function of Δb are provided, along the radial section of $i\Delta b$ = 0°. Results of q are presented on two different radii; on $r = r_c$ = 0.20 m on the wave generation circle, and on r = 0.40 m (2 x r_c). The target value of q ($q_{,target}$) is 1.0 and is obtained for $a_{r,M}$ = $a_{r,W}$. A non-linear regression (power law) has been applied through the data. As mentioned in Section 3, the grid cell discretization along the wave generation circle (which changes when the wave generation radius is modified) may affect the radius selection.

The determination coefficient R^2 equals 0.9975 and 0.9934, which confirms that the regression lines (Eqs. (9) and (10), respectively) approximate well the data points on $r = r_C$ = 0.20 m and on r = 0.40 m, respectively.

$$q = 1.903\ \Delta b^{-0.760}, \qquad \text{on } r = r_C = 0.20 \text{ m} \tag{9}$$

$$q = 2.049\ \Delta b^{-0.968}, \qquad \text{on } r = 0.40 \text{ m} \tag{10}$$

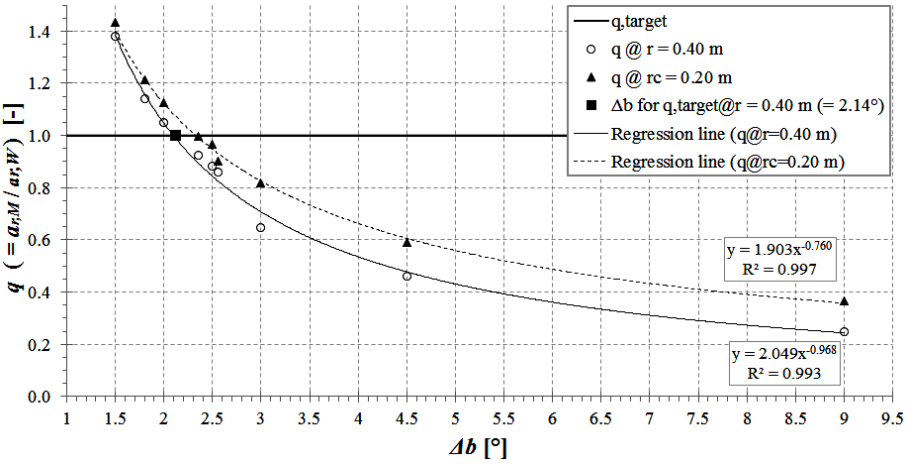

Figure 10. Ratio q (= $a_{r,M}$ / $a_{r,W}$) as a function of Δb, for regular wave generation on a circle with r_C = 0.20 m. q is calculated for two radii around the WEC: $r = r_C$ = 0.20 m ("triangle"-symbols) and r = 0.40 m ("circle"-symbols). The target value of q ($q_{,target}$) is indicated at value 1.0 (thick continuous horizontal line). The resulting Δb (=2.14°) for achieving $q_{,target}$ is indicated using a "square"-symbol. The regression lines of the q-values for $r = r_C$ = 0.20 m (thin dashed line) and for r = 0.40 m (thin continuous line) are also shown.

In Fig. 10, as Δb increases (>2.35°), q becomes too low and therefore the generated $a_{r,M}$ along a wave generation circle do not reach the target wave amplitude values $a_{r,W}$ which are derived from WAMIT and used as input on the wave generation circle. On the other hand, very small Δb values (< 2.00°) result in the generation of too high wave amplitudes, $a_{r,M}$, especially in the vicinity of the wave generation circle. Nevertheless, in the following sections, the agreement between MILDwave and WAMIT results for wave amplitudes will not be investigated on the wave generation circle, but further from the WEC and specifically at radii ≥ 0.40 m. Therefore, as shown in Fig. 10, Δb should be between 2.0° and 2.35°, in order to achieve $q_{,target}$. It is found that Δb = 2.14°, which derives from the q values on r = 0.40 m in Fig. 10. Consequently, Δb = 2.14° is used for generating radiated waves around the WEC, by applying the technique described in Section 3.1.2.2.

4.4 PERTURBED WAVE FIELD MODELED IN WAMIT AND IN COUPLED MILDWAVE

The resulting wave amplitude, a, of the perturbed wave field, is shown in Fig. 11, when simultaneously diffraction and radiation caused by the incident waves are considered. Figure 11a presents results from WAMIT, while Figure 11b presents results from MILDwave with the coupling methodology implemented (or else “coupled MILDwave”). The WEC is implemented as a fully reflecting heaving structure, placed in the centre of the numerical domain. Here numerical domains with extended dimensions are presented, 49.6 m x 39.2 m (w_d x l_d).

In Fig. 11, the incident waves propagate from the bottom to the top, and simultaneously, radiated waves propagate in all directions from the source (WEC). The resulting perturbed wave field around the WEC is similar to the diffracted wave field of Fig. 8. However, in Fig. 11, the wave amplitudes in the lee of the WEC appear to have larger variation and receive higher values. Specifically, the wave amplitudes are increased and this increase remains visible at larger distances. Moreover, the local peak of wave amplitude in front of the WEC due to wave reflection shown in Fig. 11, is now less present compared to Fig. 8, and a new peak is dominating in the lee of the WEC. The results for a and φ in the circular area with radius $r < r_C$ and (x_C, y_C) in the centre of the domain in MILDwave, are set to zero, similarly to Section 4.2; the values within the wave generation circle have no physical meaning, as this area corresponds to the circular wave absorbing sponge layer of Fig. 2b.

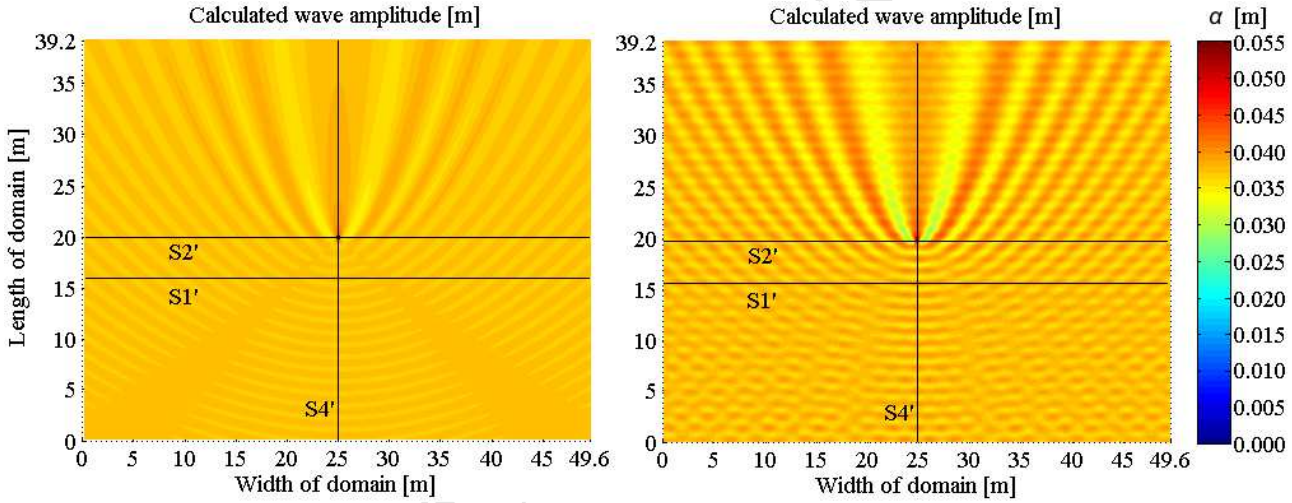

(a) WAMIT: wave amplitude, a. (b) Coupled MILDwave: wave amplitude, a.

Figure 11. Calculated wave amplitude, a, for the perturbed wave field around a heaving WEC for a domain with extended dimensions, 49.6 m x 39.2 m (w_d x l_d). Incident waves, generated along a wave generation line, propagate from the bottom to the top, and radiated waves (in MILDwave these are generated along a wave generation circle), propagate in all directions from the source (WEC), simultaneously. (a) WAMIT; (b) MILDwave with the coupling methodology implemented.

For the calculation of the perturbed wave field in MILDwave, an additional phase shift, φ, between the radiated and diffracted wave field is obtained from the WAMIT results. A longitudinal section through the WEC at x^* = 24.8 m is considered in the WAMIT numerical domain, taking into account only the area downwave of the WEC (Fig. 12). In this longitudinal section, the radiated and diffracted wave have the same direction of wave propagation. From Fig. 12 it is seen that an additional phase shift, $\Delta\varphi$ = 0.53 rad (30.5°) is needed between the radiated and the diffracted wave, to model the perturbed wave field in the coupled MILDwave.

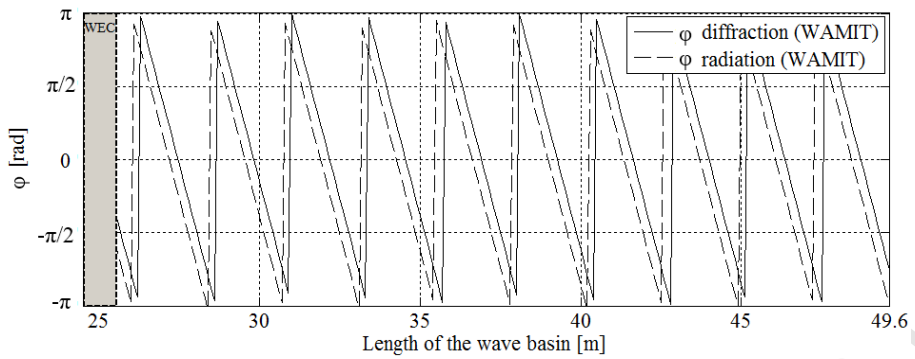

Figure 12. Difference between phase shift (relative to the centre of the WEC) of the radiated and diffracted wave field, as simulated using WAMIT.

5 VALIDATION OF THE PROPOSED COUPLING METHODOLOGY

5.1 PRESENTATION OF VALIDATION RESULTS

For the validation of the obtained results using the coupled MILDwave, the results from WAMIT are used as reference. WAMIT is a widely used and established code in the field of wave energy and naval engineering, and is extensively used as a stand-alone numerical solver in the literature. To make a detailed comparison, cross sections at several distances from the centre of the WEC are studied, showing wave amplitude, a, results. The locations of these cross sections (S1-S6) are indicated on the contour plots presented in the previous sections. For the sake of simplicity, here are presented only the lateral sections in front of (S1) and through (S2) the WEC, at respectively y^* = 0.5 m and 5.0 m. Also only the longitudinal sections at the side (S6) and through (S4) the WEC are shown, at respectively x^*= 5.0 m and 9.5 m. These sections are identified as the most important ones.

In addition, results of the obtained wave amplitudes, a, and phase shifts, φ, are compared, on a circular section around the WEC with r = 0.40 m >r_C = 0.20 m.

Values of absolute differences of wave amplitude, a, between WAMIT and the coupled MILDwave are also shown, in terms of 100 % percentages and are calculated as:

$$d_{(M-W)} = \left|\frac{a_M - a_W}{a_W}\right| . 100\ \% \qquad (11)$$

where a_M and a_W are the wave amplitudes calculated in MILDwave and in WAMIT, respectively.

5.2 VALIDATION OF THE DIFFRACTED WAVE FIELD

In Figures 13(a-b-c-d), the calculated wave amplitude, a, for the incident and diffracted wave field in WAMIT and MILDwave are compared in cross sections indicated on Fig. 8. The location of the WEC in the considered 10.0 m x 10.0 m numerical domain is also indicated. In Fig. 14 the obtained wave amplitudes, a, and phase shifts, φ, are compared on a circular section around the WEC with r = 0.40 m.

Very good agreement is observed, while the differences, $d_{(M-W)}$, between the wave amplitudes, a, calculated using WAMIT and MILDwave do not exceed 4.1 % in the entire domain. This largest difference is observed in S4 just in front of the WEC, showing that the modeled WEC exhibits in MILDwave higher wave reflection. Small deviations are seen in the lee of the WEC in S4, reaching 3.6 %. In the area in front of the WEC, the largest differences are observed within the zone at the sides of the WEC (at a distance of ± 1.0 m) where these reach 2.6 % (S1), due to higher wave reflection by the WEC in MILDwave. Also in Figures 14(a-b) very good agreement is observed between the two models.

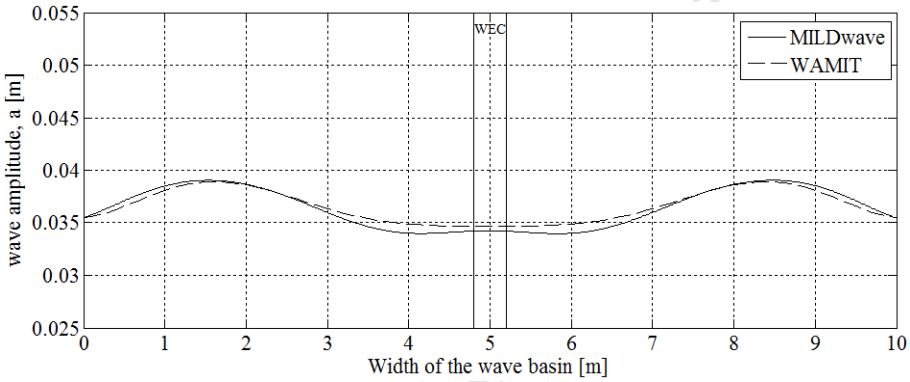

(a) Section S1.

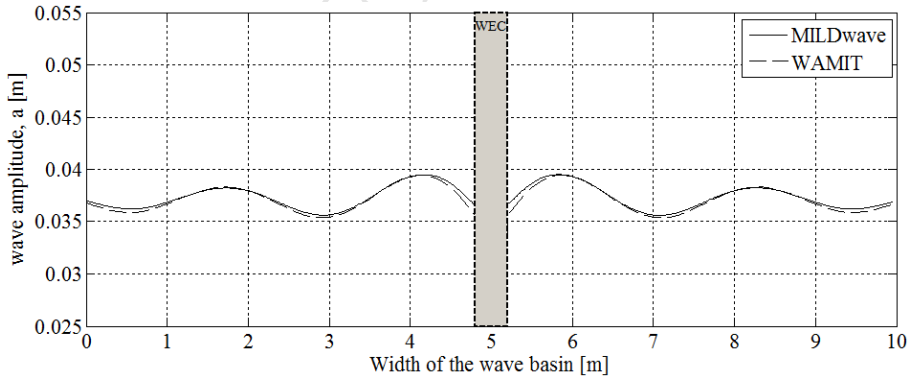

(b) Section S2.

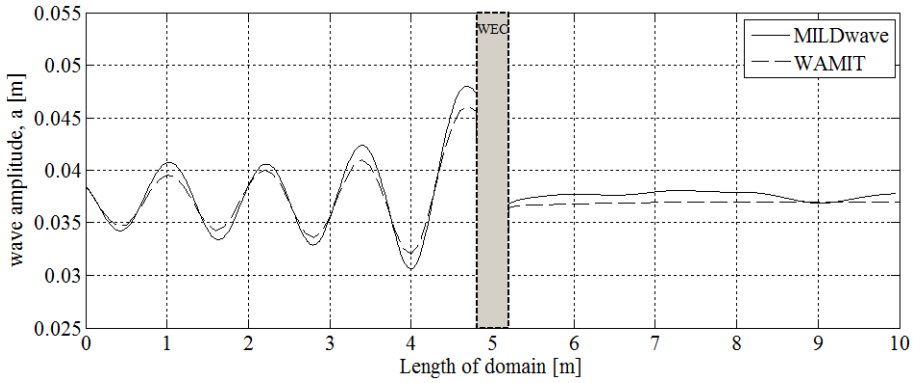

(c) Section S4.

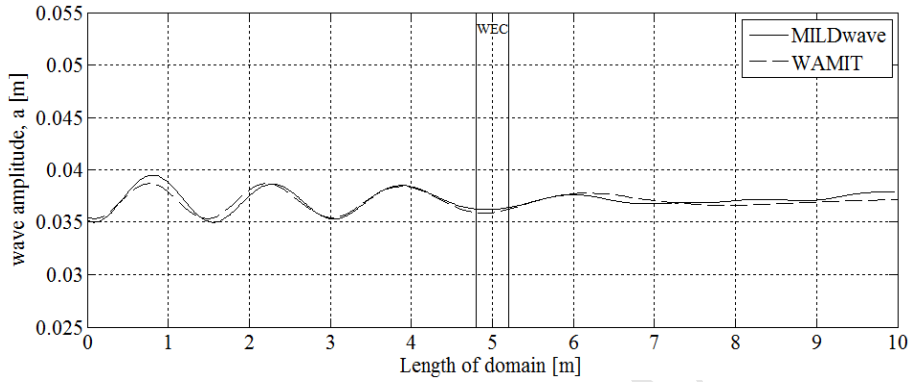

(d) Section S6.

Figure 13. Comparison between WAMIT and MILDwave results, by presenting the calculated wave amplitude, a, in the lateral sections (a) S1 and (b) S2, and in the longitudinal sections (c) S4 and (d) S6. These are a results for incident and diffracted wave field.

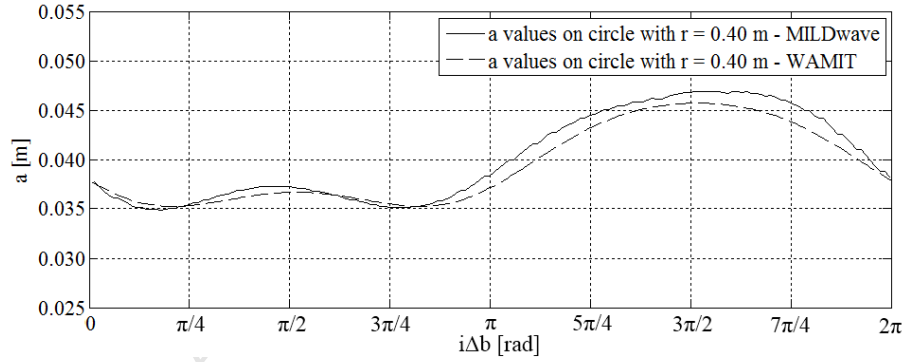

(a) wave amplitude, a.

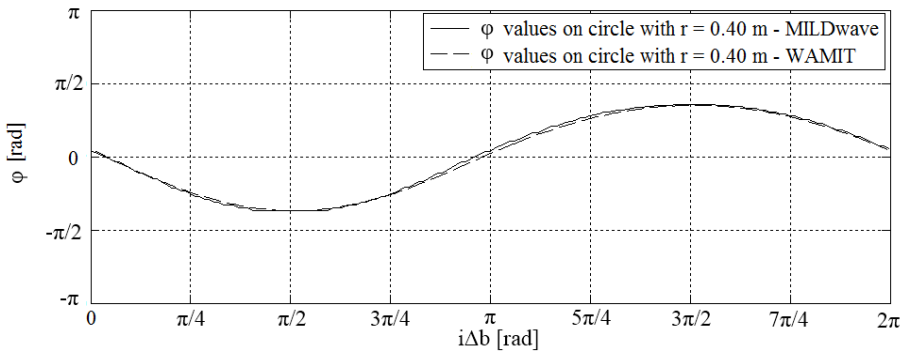

(b) phase shift, φ.

Figure 14. Comparison between WAMIT and MILDwave results, by presenting the wave amplitude, a, and phase shift, φ, on a circle of radius, r = 0.40 m and with a centre that coincides with the centre of the WEC. These are results for incident and diffracted wave field.

5.3 VALIDATION OF RADIATED WAVE FIELD USING THE INTERNAL WAVE GENERATION ALONG A CIRCLE

In Figures 15(a-b-c), the calculated wave amplitudes, a, for the radiated wave field in WAMIT, and in MILDwave where the internal circular wave generation boundary is used, are compared in three longitudinal sections (S4, S5, S6, indicated on Figures 9(a-b). For the sake of simplicity, the lateral sections (S1, S2, S3) are not plotted separately, as the radiated wave field around the axi-symmetric WEC is also axi-symmetric.

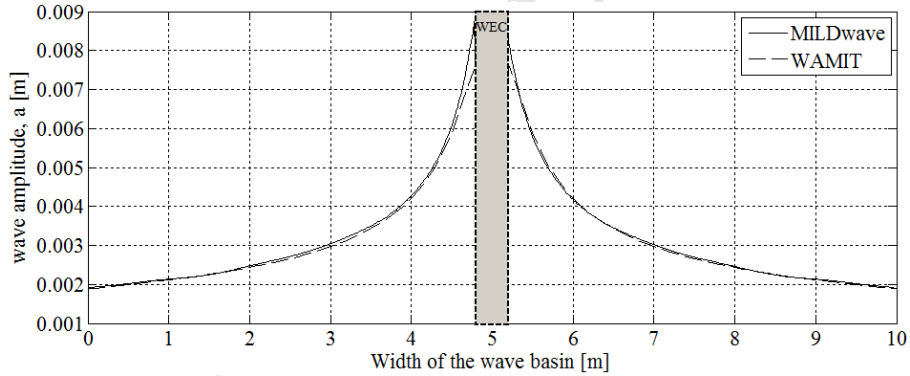

(a) Section S4 = Section S2 due to axi-symmetric radiated wave field around an axi-symmetric WEC.

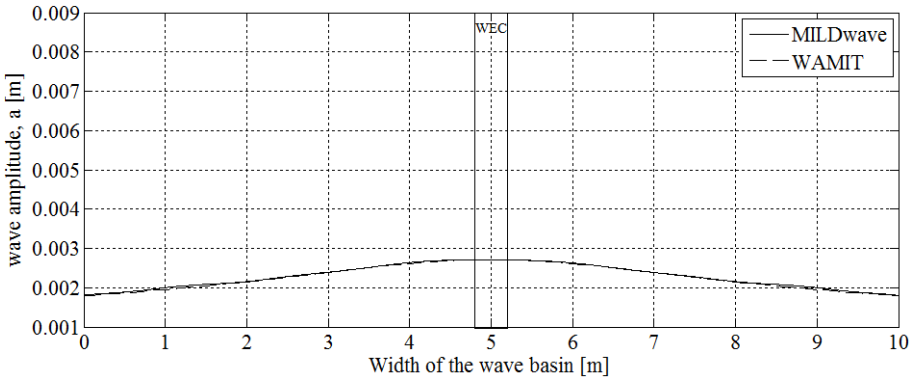

(b) Section S5.

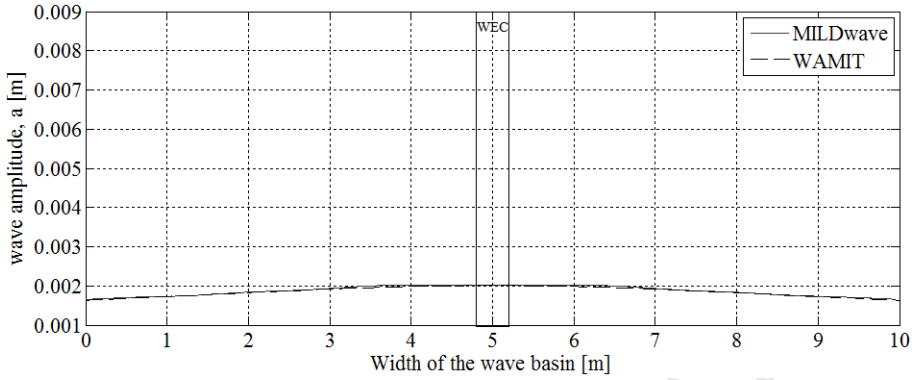

(c) Section S6 = Section S1 = Section S3 due to axi-symmetric radiated wave field around an axi-symmetric WEC.

Figure 15. Comparison between results from WAMIT, and MILDwave (where the internal circular wave generation boundary is used), by presenting the calculated wave amplitude, a, in the lateral sections (c) S1, (a) S2 and (c) S3, and in the longitudinal sections (a) S4, (b) S5 and (c) (S6). These are a results for radiated wave field.

Very good agreement is observed, with the WAMIT and MILDwave results hardly being distinguished from each other. Very small deviations are seen only on the wave generation circle, in the cross sections through the WEC (section S2 and section S4), however, these results are not taken into account for this comparison.

Moreover, the obtained wave amplitudes, a, and phase shift, φ, are compared on a circular section around the WEC with r = 0.4 m (Figure 16). Also those results show very good agreement, confirming the accuracy of the implemented wave generation technique in MILDwave, for generating waves on an internal circular wave generation boundary.

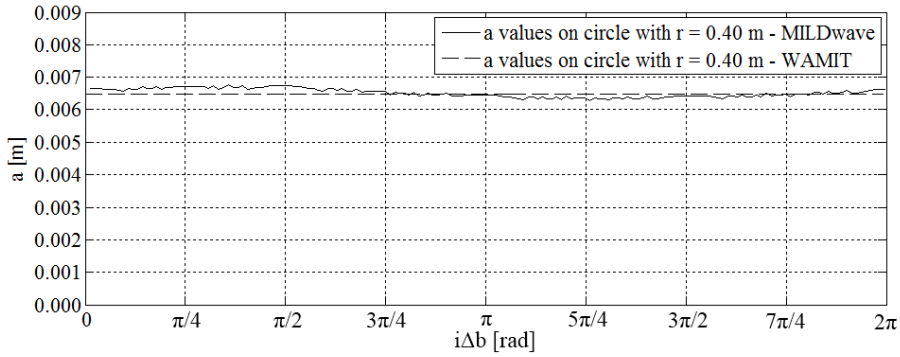

(a) wave amplitude, a.

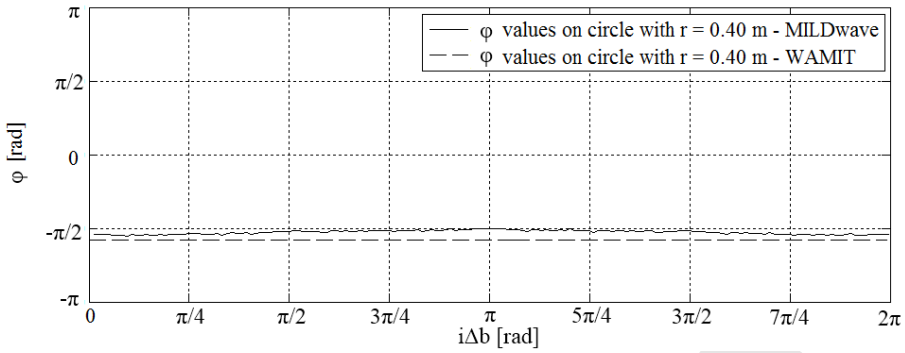

(b) phase shift, φ.

Figure 16. Comparison between results from WAMIT and MILDwave (where the internal circular wave generation boundary is used), by presenting the wave amplitude, a, and phase shift, φ, on a circle of radius, r = 0.40 m and with a centre that coincides with the centre of the WEC. These are results for radiated wave field.

5.4 VALIDATION OF PERTURBED WAVE FIELD USING THE COUPLING METHODOLOGY

In Figures 17(a-b-c-d), the calculated wave amplitudes, a, are compared for the perturbed wave field in WAMIT, and in the coupled MILDwave, in two lateral sections (S1' and S2') and one longitudinal section (S4') of the extended numerical domains, as noted in Figure 11. The location of the WEC in the presented 49.6 m x 39.2 m numerical domains is also indicated. As mentioned by Babarit (2013) the device performance becomes practically independent of the spacing for separating distances greater than 4 radii. Therefore, by pursuing an "engineering" approach, a near-field area around the WEC is considered, in which the coupled MILDwave results will not be used. Based on practical considerations, this area is taken equal to the surface area of a circle with radius $5D$ (D is the WEC diameter, where here $5D$ = 5 x (0.315 m) = 1.575 m), conventionally used as the shortest WEC-to-WEC distance in a number of numerical and experimental studies of WEC arrays (Babarit, 2013; Stratigaki et al., 2014). The hatched area shown at the sides of the WEC (in S1', S2'), as well as upwave and downwave (in S4') of the WEC, represents then this area around the

WEC with radius ($x_C \pm 5D$) or ($y_C \pm 5D$). Outside the hatched area, coupled MILDwave results will be compared to WAMIT results to evaluate the achieved accuracy of the proposed coupling methodology. For largely spaced WEC arrays the hatched may be even larger.

Moreover, in Figure 18, the obtained values of phase shift, φ, using the coupled MILDwave are compared to WAMIT results for φ, on a circular section of r = 0.40 m around the WEC.

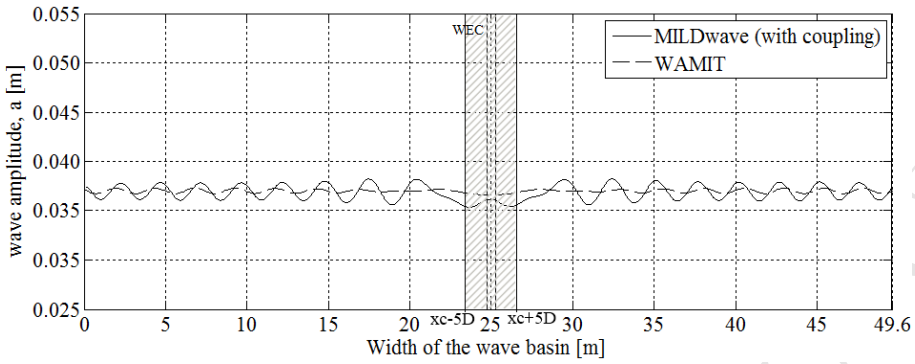

(a) Section S1'.

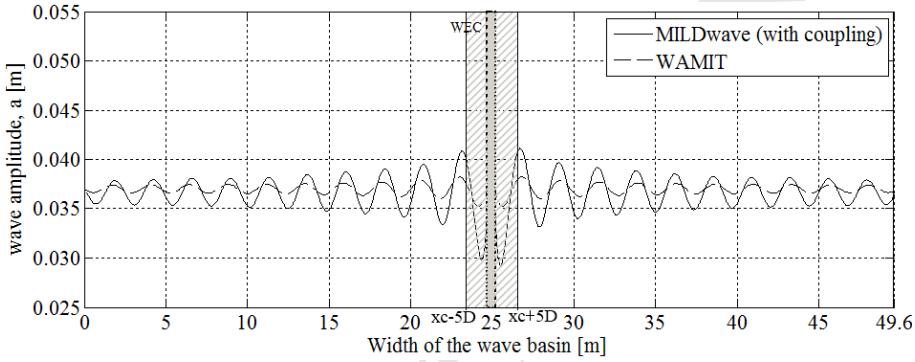

(b) Section S2'.

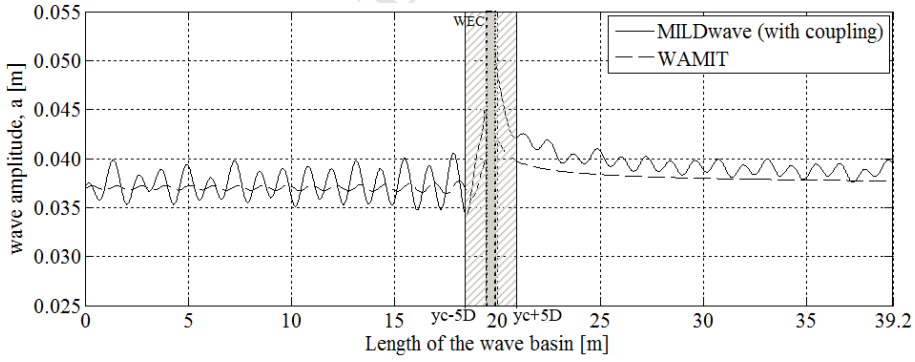

(c) Section S4'.

Figure 17. Comparison between WAMIT, and coupled MILDwave, by presenting the calculated wave amplitude, a, in the lateral sections (a) S1' and (b) S2', and in the longitudinal section (c) S4'. These are a results for the perturbed wave field. The hatched area around the WEC is also indicated, with radius ($x_C \pm 5D$) or ($y_C \pm 5D$). (x_C, y_C) is the centre of the WEC and of the wave generation circle, and D is the WEC diameter. Within this area, results are not considered.

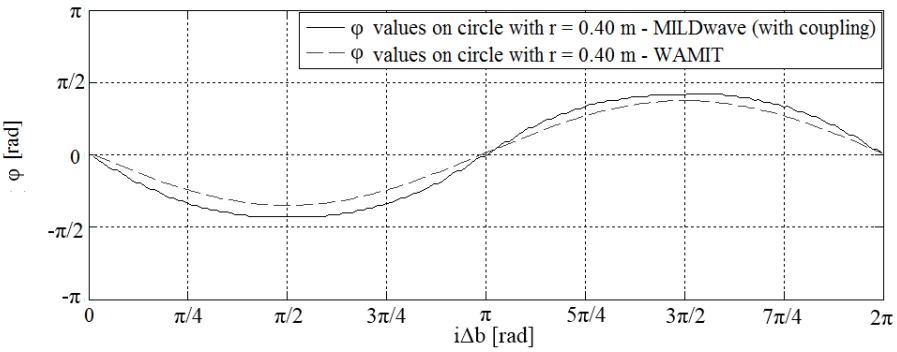

Figure 18. Comparison between results from WAMIT and coupled MILDwave, by presenting the phase shift, φ, on a circle of radius, r = 0.40 m and with a centre that coincides with the centre of the WEC. These are results for perturbed wave field.

In general, a very good agreement is observed in the far-field. The differences $d_{(M-W)}$ between the wave amplitudes, a, for the perturbed wave field, calculated using WAMIT and the coupled MILDwave do not exceed in S1' the value of 3.3 %. The largest difference at the far-field, reduces to 1.8 % as shown in S1' (i.e. at distance x = 0.0 m and x = 49.6 m in the domain width).

In S2', the largest $d_{(M-W)}$ value appears at x_C ± 0.4 m from the WEC centre and is a very localized effect. However, only results within radii larger than r = 0.4 m from the WEC centre are taken into account in the comparisons. This is because results from grid points within radii smaller than r = 0.4 m are considered to be too close to the wave generation circle. In addition, this largest $d_{(M-W)}$ at x_C ± 0.4 m is situated within the hatched area around the WEC, with radius x_C ± 5D, where again the obtained results are not used for comparison.

In S2', and a little further from the WEC centre, at x_C ± 1.7 m and at x_C ± 3.0 m, the $d_{(M-W)}$ values reduce to 7.3 %, while the largest difference at the far-field reducing to 3.1 % (i.e. at distance x^*= 0.0 m and x^* = 49.6 m in the domain width).

In S4', the largest $d_{(M-W)}$ value appears in the lee of the WEC, at a distance of 0.2 m from the WEC centre, and is a very localized effect. This high difference appears, though, on the wave generation circle, where the wave amplitude differences are not taken into account for this comparison. As shown in S4', in the lee of the WEC and right after 1.0 m from the WEC centre, those differences are 6.9 % (which lies within the hatched area of (y_C + 5D), and so not to be used for comparison), and reduce to 0.0 % - 5.7 % in the far-field (i.e. at distance x^* = 39.2 m in the domain length). In the same section S4' and in front of the WEC, the largest differences appear again on the wave generation circle, and these results are not taken into account in the presented

767 comparisons. These differences reduce to 0.8 - 7.1 % at the far-field, as shown in S4' (i.e. at
768 distance x^* = 0.0 m in the domain length).
769 Also in Figure 18, acceptable agreement is observed between the two models for the phase shifts
770 (relative to the centre of the WEC), on a circle with r = 0.40 m. However, there are differences,
771 especially in the lee (at $i\Delta b = \pi/2$) and at the front (at $i\Delta b = 3\pi/2$) of the WEC. These differences in
772 the phase shifts, φ, are also responsible for the wave amplitude differences.
773 In order to make a detailed results' evaluation, also the $d_{(M-W)}$ values over the entire domains are
774 shown in Figure 19, for the 49.6 m x 39.2 m numerical domain. In this way, a clear overview is
775 given, of the spatial variability of the wave amplitude differences in the entire domain, mainly
776 focusing on the far field effects.

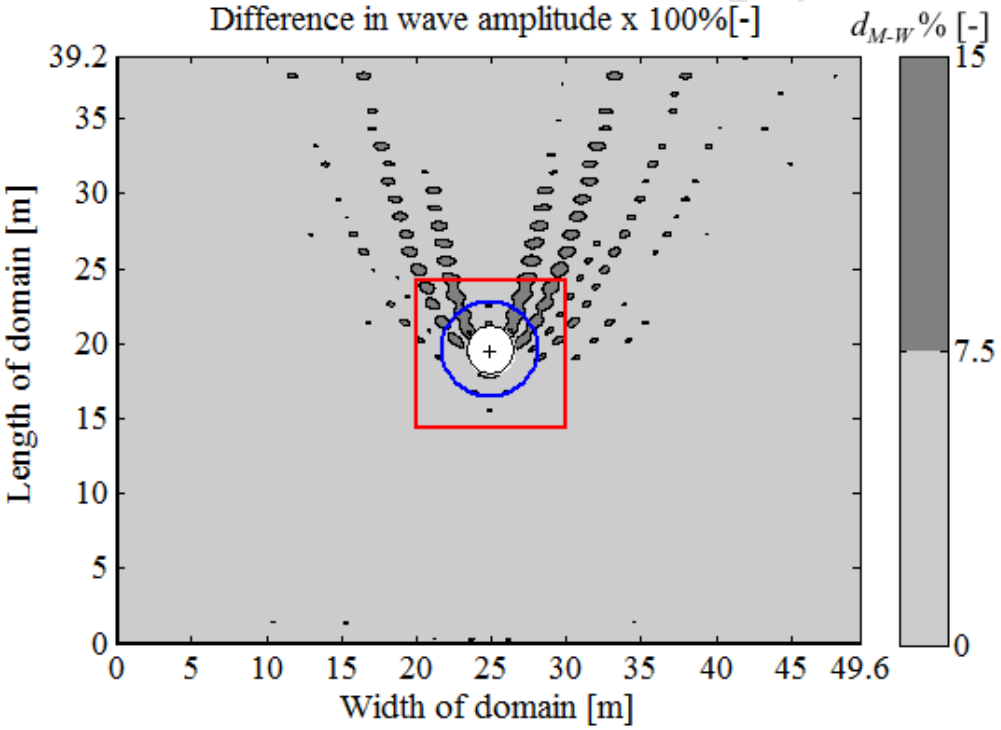

777
778 **Figure 19.** Calculated (using Eq. (11)) wave amplitude differences $d_{(M-W)}$ between the coupled MILDwave and
779 WAMIT, for the perturbed wave field around a heaving WEC. An extended domain with dimensions, 49.6 m x 39.2 m
780 (w_d x l_d) is shown. Light grey and grey colour, represent areas with differences smaller than 7.5 % and between 7.5 %
781 and 15.0 %, respectively. The zones within the drawn inner (solid white) and outer (hollow blue) circles are indicated,
782 with radii 5D and 10D, respectively, where D is the WEC diameter. The "+"-symbol indicates the WEC centre. The
783 drawn red square indicates the spatial limits of a 10.0 m x 10.0 m area.
784
785 In order to visualize the effect of these differences for the studied test case, two circles have been
786 drawn in Figure 19. The centres of the circles coincide with that of the WEC. The radius of the
787 inner circle is equal to 5D, and within this area the results are not used for performance comparison
788 between the two models (this is the hatched area of Fig. 17). As also shown in the cross sections of

Figure 17, the largest wave amplitude differences remain within this circular area of radius $5D$. As a result, when additional WECs would be added at a distance of $5D$ in front of and/or in the lee of the WEC in order to create a WEC array, the largest wave amplitude differences that these new WEC(s) will experience when the coupled MILDwave is used, do not exceed 8.0 %. We would like to point out that the differences reported here are based on the coupling between the two linear models employed for this study, WAMIT and MILDwave. Therefore, the validity of these differences refer to this type of coupling, and especially to applications for which linear theory is suitable as e.g. reported by Folley et al. 2012. When the use of linear models is not applicable anymore, because e.g. non-linear phenomena are significant, then coupling of non-linear models is suggested (i.e. between a non-linear wave-structure interaction solver and a non-linear wave propagation model). Moreover, regular waves (used in the present study) may result into higher differences compared to realistic sea-states of short-crested irregular waves, where both near-field and far-field effects of such heaving WECs are limited, as presented by Stratigaki et al. 2014. This wave amplitude difference of 8.0 % represents two local peaks in front of and in the lee of the WEC, as shown in detail in Figure 17. Moreover, as presented in Figure 19, the largest $d_{(M-W)}$ values (16.5 %) appear in the lee sides of the WEC at ± 45° (plan view), and are spatially very limited and localized effects, with the differences in this limited zone varying between 7.5 % and 15.0 %. Yet, in the largest part of the domain, and especially in front of and in the lee of the WEC, the $d_{(M-W)}$ values are small (<7.5 %) which shows the good agreement between the results obtained using WAMIT and coupled MILDwave.

In Figure 19, also a second circle is drawn (the outer red circle) with a radius of $10D$, representing a typical WEC-to-WEC distance between the WECs of an array. This distance is proposed by Babarit (2013), who found that near-field effects are no longer important and can be neglected for a WEC spacing larger than $10D$. As shown in Figure 19, the largest wave amplitude differences remain in an area within this circle of diameter $10D$. As a result, the coupling methodology implemented in MILDwave can be used to model WEC arrays with spacing between the WECs equal and larger than $10D$, installed e.g. in front of and/or in the lee of the WEC shown in Figure 19. In that case, the largest $d_{(M-W)}$ values that the additional successive WEC(s) may experience are small, and do not exceed the 7.5 %, while at the largest part of the domain they are smaller than 5.0 %.

Therefore, the coupling methodology implemented in the wave propagation model MILDwave is suitable for modelling WEC far field effects, with the wave amplitude differences being very small,

especially in front and in the lee of the WEC. This confirms the good agreement between the results obtained using WAMIT and the coupled MILDwave.

6 SUMMARY & CONCLUSIONS

This study focuses on the numerical modeling of wave field modifications around floating structures. Especially for the case of wave energy converters, the aim is to model near and far field WEC effects. The proposed methodology is also suitable for a pair of WECs and can be used for a WEC array or farm.

A generic coupling methodology is developed to combine: (a) the approach of wave-structure interaction solvers, which are used to investigate near field effects. These can more correctly model wave energy absorption (in the case of WECs) and the wave fields induced by floating bodies; and (b) the approach of wave propagation models, which are used for predicting far field effects. These can model the impact of WECs on the surrounding wave field and on the shoreline.

In addition, a novel wave generation technique is presented, which is used in a wave propagation model for the perturbed wave field induced by a floating structure or energy device. A wave generation circle is employed, which surrounds the WEC, and on which prescribed internal boundary wave conditions are imposed. These input wave conditions are provided by a wave-structure interaction solver.

One of the main advantages of the proposed coupling methodology and the wave generation technique on a circle, is that both are generic:

(i) any wave-structure solver can be used to provide the perturbed wave field, which is used to prescribe input wave conditions on the internal boundary (on a wave generation circle) of the wave propagation model.

(ii) any wave propagation model (both phase resolving and phase averaging models) can be used;

(iii) it applies to any oscillating/floating body, e.g. to offshore structures, WECs, oscillating water columns, floating breakwaters, platforms, etc.

(iv) by using this coupling methodology, it is possible to model the resulting wave fields around rigid structures which have from 0 (fixed) up to all 6 DOFs.

Verification of the presented coupling methodology is performed using a test case of a heaving WEC, for which coupling between the wave-structure interaction solver, WAMIT, and the time domain wave propagation model, MILDwave, has been demonstrated. The results obtained for the diffracted, radiated and perturbed wave fields around the WEC, using the coupling methodology,

have been verified against the results obtained by WAMIT. Furthermore, MILDwave can provide results at larger distances downwave of the WEC in a time-effective way, using the actual bathymetry of the domain, which is not possible in WAMIT.

When only diffraction is considered, the resulting wave amplitudes in WAMIT and in MILDwave show very good agreement.

When only radiation is considered, the resulting wave amplitudes in WAMIT and in MILDwave show very good agreement (they are almost identical). In MILDwave, radiated waves are generated along the employed wave generation circle which surrounds the WEC. The prescribed internal boundary wave conditions on the circle are provided by WAMIT, and the WEC has been implemented as a wave source.

Diffraction and radiation are considered simultaneously in MILDwave by applying the presented coupling methodology, are compared to WAMIT results. The resulting wave field is the perturbed wave field around the heaving WEC under incident waves.

In MILDwave, each time step, the diffracted and radiated wave field are calculated separately and afterwards the wave elevations and velocity potentials are summed up.

The WEC is implemented as an oscillating fully reflecting structure surrounded by the wave generation circle, and is placed in the centre of the numerical domain. Waves are simultaneously generated along a wave generation line at the offshore boundary, and along a wave generation circle.

The perturbed wave field results using WAMIT, and the coupled MILDwave, model show very good agreement. The largest wave amplitude differences appear to be very localized effects at very small distances around the WEC and on the wave generation circle. However, these areas are not considered for the results' comparison. The wave amplitude differences are smaller than 7.5 % and even smaller than 5.0 % in the majority of the numerical domain. In particular, in front of the WEC, in the lee of the WEC and in the far field. This shows the good agreement between the results obtained using WAMIT and the coupled MILDwave model. Therefore, the proposed coupling methodology is suitable for simulating far field effects of the modeled WEC.

In this study, it has been shown that the proposed numerical coupling methodology for predicting WEC effects, can combine **(i)** the advantages of wave-structure interaction solvers, and **(ii)** the benefits of wave propagation models, yielding a cost-effective and more accurate tool.

ACKNOWLEDGMENTS

The first author would like to acknowledge her Ph.D. funding grant by the Research Foundation Flanders (FWO), Belgium. This research is also supported by FWO.OPR.2.0l—FWO research project No. 3G029114.

REFERENCES

Agamloh, E.B., Wallace, A.K., von Jouanne, A., 2008. Application of fluid-structure interaction simulation of an ocean wave energy extraction device. Renewable Energy. 33(4), 748-757.

Alexandre, A., Stallard, T.J., Stansby, P.K., 2009. Transformation of wave spectra across a line of wave devices. Proceedings of 8th European Wave & Tidal Energy Conference (EWTEC), Uppsala, Sweden.

ANSYS Aqwa, Product features, http://www.ansys.com

Babarit, A., Folley, M., Charrayre, F., Peyrard, C., Benoit, M., 2013. On the modeling of WECs in wave models using far field coefficients. Proceedings EWTEC2013, Aalborg, Denmark.

Babarit, A., 2013. On the park effect in arrays of oscillating wave energy converters. Renewable Energy. 58, 68-78.

Babarit, A.; Delhommeau, G. Theoretical and numerical aspects of the open source BEM solver NEMOH. In Proceedings of the 11th European Wave and Tidal Energy Conference, Nantes, France, 6–11 September 2015.

Beels C. Optimization of the lay-out of a farm of wave energy converters in the North Sea: analysis of wave power resources, wake effects, production and cost. [Ghent, Belgium]: Ghent University. Faculty of Engineering; 2009.

Beels, C., Troch, P., De Visch, K., Kofoed, J.P., De Backer, G., 2010a. Application of the time-dependent mild-slope equations for the simulation of wake effects in the lee of a farm of Wave Dragon wave energy converters. Renewable Energy. 35, 1644-1661.

Beels, C., Troch, P., Kofoed, J.P., Frigaard, P., Vindahl Kringelum, J., Carsten Kromann, P., Heyman Donovan, M., De Rouck, J., De Backer, G., 2010b. A methodology for production and cost assessment of a farm of wave energy converters. Renewable Energy.36(12), 3402-3416.

Beels, C., Troch, P., De Backer, G., Vantorre, M., De Rouck, J., 2010c. Numerical implementation and sensitivity analysis of a wave energy converter in a time-dependent mild-slope equation model. Coastal Engineering, 57(5), 471-492.

Booij, N., Haagsma, I.J.G., Holthuijsen, L.H., Kieftenburg, A.T.M.M., Ris, R.C., van der Westhuysen, A.J., Zijlema, M., 2007. SWAN cycle III version 40.51AB User Manual.

Chang, G., K. Ruehl, C.A. Jones, J. Roberts, C. Chartrand, 2016. "Numerical modeling of the effects of wave energy converter characteristics on nearshore wave conditions." Renewable Energy 89 (2016): 636-648.

Crespo, A. J. C., M. Hall, J. M. Domínguez, C. Altomare, M. Wu, T. Verbrugghe, V. Stratigaki, P. Troch, and M. Gómez-Gesteira. 2018. “Floating Moored Oscillating Water Column With Meshless SPH Method.” In Proceedings of OMAE-2018. ASME. http://dx.doi.org/10.1115/omae2018-77313

De Backer, G., Vantorre, M., Beels, C., De Rouck, J., Frigaard, P., 2010. Power absorption by closely spaced point absorbers. IET Renewable Power Generation. 4(6), 579-91.

Delhommeau, G., 1987. Le problème de diffraction radiation et de résistance de vagues : étude théorique et résolution numérique par la méthode des singularités, Thèse Ecole Nationale Supérieure de Mécanique, Nantes.

Devolder, B.; Stratigaki, V.; Troch, P.; Rauwoens, P. CFD Simulations of Floating Point Absorber Wave Energy Converter Arrays Subjected to Regular Waves. Energies 2018, 11, 641.

Falnes, J., 1997. Principles for capture of energy from ocean waves. Phase control and optimum oscillation. Technical report, Department of Physics, NTNU.

Finnegan,W., Goggins, J., 2012. Numerical simulation of linear water waves and wave–structure interaction. Ocean Eng. 43, 23-31.

Folley, M., Babarit, A., O' Boyle, L., Child, B., Forehand, D., Silverthorne, K., Spinneken, J., Stratigaki, V., Troch, P., 2012. A review of numerical modeling of wave energy converter arrays, Proceedings of the 31st International Conference on Offshore Mechanics & Arctic Engineering, Rio de Janeiro, Brazil.

González-Santamaría, R., Zou, Q., Pan, S., 2012. Modelling of the impact of a wave farm on nearshore sediment transport. Proceedings of the 33rd International Conference on Coastal Engineering (ICCE2012), Santander, Spain.

Le Crom, I., Brito-Melo, A., Sarmento, A.J.N.A., 2008. Maritime Portuguese Pilot Zone for Wave Energy Conversion: Modelling Analysis of the Impact on Surfing Conditions. Proceedings of the 2nd International Conference on Ocean Energy (ICOE), Brest, France.

Lee, C., Suh, K.D., 1998. Internal generation of waves for time-dependent mildslope equations. Coastal Engineering. 34, 35–57.

Lee, C., Yoon, S., 2007. Internal generation of waves on an arc in a rectangular grid system. Coastal Engineering. 54, 357–368.

Li, Y., Yu, Y.-H., 2012. A synthesis of numerical methods for modeling wave energy converter point absorbers. Renewable & Sustainable Energy Reviews. 16.6, 4352-4364.

Luczko, E., Bryson, R., Bailey, H., Hiles, C., Buckhama, B., 2018. Representing non-linear wave energy converters in coastal wave models, Renewable Energy, Volume 118, April 2018, Pages 376-385, https://doi.org/10.1016/j.renene.2017.11.040.

Madsen, P.A., Sørensen, O.R., 1992. A new form of the Boussinesq equations with improved linear dispersion characteristics. Part 2: A slowly-varying Bathymetry. Coastal Eng. 18, 183-204.

Mavrakos, S., McIver, P., 1997. Comparison of methods for computing hydrodynamic characteristics of arrays of wave power devices. Applied Ocean Research, 19, 283-91.

Mei, C.C., Stiassnie, M., Yue, D.K.P., 2005. Theory and applications of ocean surface waves. Part 1, Linear aspects. World Scientific, Singapore.

Mendes, L., Palha, A., Conceicao, J.F., Brito-Melo, A., Sarmento, A.J.N.A., 2008. Analysis of the impact of a pilot zone for wave energy conversion offshore Portugal. Proceedings of the 18th International Offshore and Polar Engineering Conference (ISOPE), Vancouver, British Columbia, Canada.

Millar, D.L., Smith, H.C.M., Reeve, D.E., 2006. Modelling analysis of the sensitivity of shoreline change to a wave farm. Ocean Engineering. 34, 884-901.

O'Dea, Annika M., and Merrick C. Haller. 2014. "Analysis of the impacts of wave energy converter arrays on the nearshore wave climate." (2014).

Özkan-Haller, H. Tuba, Haller, M.C., McNatt, C., Porter, A., Lenee-Bluhm, P., 2017. "Analyses of wave scattering and absorption produced by WEC arrays: physical/numerical experiments and model assessment." Marine Renewable Energy. Springer, Cham, 2017. 71-97.

Ruehl, K., A. Porter, A. Posner, J. Roberts, 2013. "Development of SNL-SWAN, a validated wave energy converter array modeling tool." Proc. 10th Eur. Wave Tidal Energy Conf., Aalborg, Denmark. 2013.

Troch, P., 1998. MILDwave – A numerical model for propagation and transformation of linear water waves. Internal Report, Department of Civil Engineering, Ghent University.

Troch, P., Beels, C., De Rouck, J., De Backer, G., 2010. Wake effects behind a farm of wave energy converters for irregular long-crested and short-crested waves. Proceedings of the International Conference on Coastal Engineering, No. 32 (2010), Shanghai, China. Paper #: waves.22. Retrieved from http://journals.tdl.org/ICCE/.

Radder, A.C., Dingemans, M.W., 1985. Canonical equations for almost periodic, weakly nonlinear gravity waves. Wave Motion, 7, 473-485.

Stratigaki, V. (2014). Experimental study and numerical modelling of intra-array interactions and extra-array effects of wave energy converter arrays. Ghent University. Faculty of Engineering and Architecture, Ghent, Belgium.

Stratigaki, V., Troch, P., 2012. An introduction to the wave propagation model MILDwave. Department. of Civil Engineering, Ghent University.

Stratigaki, V., Troch, P., Baelus, L., and Keppens, Y., 2011. Introducing wave regeneration by wind in a mild-slope wave propagation model, MILDwave, to investigate the wake effects in the lee of a farm of wave energy converters. Proceedings *of* the ASME 2011 30th International Conference on Ocean, Offshore and Arctic Engineering (OMAE 2011). Rotterdam, The Netherlands.

Venugopal, V., Smith, G.H., 2007. Wave climate investigation for an array of wave power devices, Proceedings of the 7th European Wave and Tidal Energy Conference (2007), Porto.

Verao Fernandez, G.; Balitsky, P.; Stratigaki, V.; Troch, P. Coupling Methodology for Studying the Far Field Effects of Wave Energy Converter Arrays over a Varying Bathymetry. Energies 2018, 11, 2899.

Vicente, P.C., de O. Falcão, A.F., Gato, L.M.C., Justino, P.A.P., 2009. Dynamics of arrays of floating-point absorber wave energy converters with inter-body and bottom slack-mooring connections. Applied Ocean Research. 31, 267-81.

Vidal, C. , Mendez, F. J., Diaz, G., Legaz, R., 2007. Impact of Santona WEC installation on the littoral processes. Proceedings of the 7th European Wave and Tidal Energy Conference (EWTEC), Porto, Portugal.

WAMIT, User Manual. http://www.wamit.com/manual.htm.

Wang, H. 1986. Calculation of Far Field Radiation and Diffraction Wave Patterns Using the Kochin Function Approach for a Series of Ship Hulls. Naval Research Laboratory, Washington DC.

Westphalen, J., Greaves, D., Williams, C., Taylor, P., Causon, D., Mingham, C., Hu, Z., Stansby, P., B, R., Omidvar, P., 2009. Extreme wave loading on offshore wave energy devices using CFD: a hierarchical team approach. Proceedings of the 8th European Wave and Tidal Energy Conference, Uppsala, Sweden.

Yu, Y.-H., Li, Y., 2013. Reynolds-Averaged Navier-Stokes simulation of the heave performance of a tow-body floating-point absorber wave energy system. Computers & Fluids, 73, 104-114.